Paper accepted for publication in International Journal of Multiphase Flow, 127 (2020) 103236

Transient large-scale two-phase flow structures in a 3D bubble column reactor

Mojtaba Goraki Fard[1], Anton Vernet[1], Youssef Stiriba[1,*], Xavier Grau[1]

[1] ETSEQ, Departament d'Enginyeria Mecanica, Universitat Rovira i Virgili

Av. Paisos Catalans 26, 43007, Tarragona, Spain

Abstract

This paper analyses the local and time-dependent behavior of large-scale structures responsible for liquid circulation in gas-water flow of a 3-D cylindrical bubble column of high aspect ratio with a multiple orifice for uniform aeration. The large-scale flow structures play an important role in the mixing and the mass transfer while coherent structures dominate hydrodynamic characteristics of the turbulent flow field. A three-dimensional Euler-Euler large eddy simulation (LES) model was used to calculate large-scale structures and their interaction with bubbles at inlet superficial gas velocities of $U_G = 6$ and 8.4 cm/s where vortical-spiral and turbulent flow regimes occur. The two-phase model gives good agreements with experimental measurements. We use a conditional sampling procedure of liquid velocity and gas hold-up time series to identify and educe the development of coherent flow structures which consists in a pair of counter-rotating vortices convected in a staggered pattern along the column in both the vortical-spiral and central plume regions. On average, the detected instantaneous events for each template account for about 12-15 % of the data recorded and may appear simultaneously. These events produce important fluctuations in the axial liquid velocity and gas void fraction. The sampling procedure yielded the averaged topology of the three-dimensional large-scale structures which was visualized using iso-surfaces of the vorticity for different gas flow rates. The structures have spiral tube-shaped topology rotating along the column near the walls with a pair of counter-rotating cells sustained through the flow. This work provides deep insights into turbulent flow field in gas-liquid bubble column by LES and pattern recognition.

Keywords: Bubble column reactor; Large-eddy-simulation; Conditional sampling; Vortex; Large-scale structures

1. Introduction

Bubble columns are gas-liquid and gas-liquid-solid reactors used in many chemical, biotechnological and pharmaceutical industries, and other multiphase processes due to their effective mixing as well as mass and heat transfer characteristics between different phases at comparable energy consumptions relative to stirred-tanks vessels (Joshi 2001, Sokolochin et al. 2004, Mudde 2005, Jakobsen et al. 2005, and Vial and Stiriba 2013). In bubble column reactors, the gas phase is dispersed in the form of tiny bubbles in a continuous liquid phase using a gas distribution device. The flow pattern depends on many operating conditions such as the geometry, the gas distributors that control how the gas is spatially distributed and determines the primary bubble size distribution, and the gas flow rate that governs the flow regime. Furthermore, the complex interplay between operating conditions, the presence of turbulence and bubble-bubble interactions lead to extensive range of flow regimes and complex flow structures which dominate the hydrodynamic characteristics of the flow. Therefore, it is important to get a thorough understanding of the instantaneous flow structures.

Modelling of multiphase flows has been the subject of many research works and generally builds on two-fluid model, see Ishii and Hibiki 2006. It can be numerically investigated by various methods. For practically complete knowledge of the flow parameters, it is desirable to implement the DNS approach which would provide the highest resolution of the flow field around bubbles and has no dependence on modelling. However, the computational cost scales with the Reynolds number and the DNS places a large demand on computational resources (memory requirements and CPU time) on modelling large bubble column reactors. Therefore, one of the possible alternatives is to use the Euler-Euler two-fluid model coupled with the Reynolds-averaged Navier-Stokes (RANS) models or the Large Eddy Simulation (LES) models. The RANS models have performed satisfactory in many flow problems and can predict average flow field reasonably well (Mudde and Simonin 1999, Deen et al. 2001, Selma et al. 2010, Ekambara and Dhotre 2010, Masood et al. 2014), but their applicability is limited since the flow in the bubble column is anisotropic and exhibits large scale vortical structures. The LES models can be regarded as valuable and successful tools to predict flows dominated by large transient structures and permit the bubble to interact with eddies of at least the same size (Deen et al. 2001, Milelli 2002, Tabib et al. 2008, Dhotre et al. 2008, Liu and Li 2018). They offer the possibility to resolve the large scales of motion which carry most of the flow energy, while the small scales are modelled with a subgrid-scale (SGS) model. Furthermore, the LES approach is less dependent on modelling and can capture more dynamics compared to RANS models, see Dhotre et al. 2013, Zhang et al. 2006, Tabib et al. 2011.

The aim of this work is to use a conditional sampling technique based on database of LES in a 3D cylindrical bubble column reactor to extract the topology of different flow structures. The LES approach has a drawback, since the largest interface details should be smaller than the grid size for the sake of consistency. This means that the grid cell size must be larger than the bubble size and a lot of details move to SGS level in particular the bubble-induced turbulence (BIT). The effect of sub-grid scale eddies on the turbulent dispersion force is another issue that has to be incorporated in interfacial force modelling. The Smagorinsky model and the dynamic Samgorinsky model were used in many works, see for instance Zhang et al. 2008, and Ma et al. 2015, but are not able to provide explicit information of the modelled sub-grid scale. Niceno et al. 2008 proposed to employ the one-equation SGS kinetic energy LES (Davidson, 1997) to gas-liquid flows, and obtained superior results to Smagorinsky model and the dynamic model. They added a source term to the transport equation for the SGS turbulent kinetic energy to model the BIT more accurately. Furthermore, they pointed out the possibility to use information on SGS kinetic energy to quantify the SGS turbulent dispersion force. Tabib et al. 2011 use the one-equation SGS model to analyse such force on different particle systems, namely the gas-liquid bubble column and the liquid-liquid pump mixer. Therefore, the one-equation model was adopted in this work and has shown to be accurate and computationally less demanding than the RANS model.

The flow structures in bubble column reactors are characterized by the development of a spectrum of structures for transition and heterogeneous flow regimes and have been extensively studied in the published literature. For instance, Chen et al. 1994 reported that as we increase the inlet gas flow rate clusters of bubbles travel through the column center carrying the liquid in almost a spiral rotating movement and small bubbles spirally downward in the near-wall region. The general macroscopic flow structure in vortical-spiral flow regime for 3D bubble column is shown in Fig. 1 based on measurements and observations of Chen et al. 1994. As we increase the inlet superficial gas velocity the intensity of turbulence destroys the vortical and spiral structures leading to turbulent flow structures. In Joshi et al. 2002, an overview over different resolving simulations of various flow patterns is provided with a classification of different circulation cell representations as schematically shown in Fig. 2. For instance, the averaged flow pattern can be represented as a single cell liquid recirculation, see Fig. 2(a). Here we observe that the instantaneous macroscopic structures were lost when the information was time averaged. Joshi and Sharma 1979 and Joshi 1992 pointed out different instantaneous flow structures of non-interacting cells and interacting cells with considerable intercirculation as depicted in Fig. 2(b)-(c) and Fig. 2(f) respectively. The later occur for high bubble column diameters and superficial gas velocities in the range of 19-92 mm/s. Another model of multiple circulation cells which span the entire column was considered and observed by several

authors, see for instance Zehner 1992 and Chen et al. 1989, or staggered circulation cells by Jamilahmadi et al. 1989 when the aspect ratio H/D exceeds some limit, see also Fig. 2 (d)-(e).

The large-scale liquid circulation, vortical structures and their behavior are complex. Their range of existence depends mainly on the bubble column aspect ratio H/D, where H is the height and D is the width, the gas distribution type, the initial gas flow rate and the liquid properties. These flow patterns were found at different superficial gas velocities in Mudde et al. 1997, Mudde and van den Akker 1999, Chen et al. 1994, Harteveld et al. 2003, Sathe et al. 2011 and Sun et al. 2012. Furthermore, a significant amount of computational work has been done to reproduce numerically the liquid circulation and coherent structures that were found experimentally, see the works of Lapin and Lübbert 1994, Harry Van Den Akker 1998, Sokolichin et al. 1997, Bauer and Eigenberger 1999, and Simiano and Lakehal 2012. The largest flow structure (large eddy in the column) has a maximum size of the order of the column diameter, affects the local turbulence and can enhance the local transport phenomena, see Sathe et al. 2011. However, the role of uniform aeration in the dynamics of large-scale structure at high superficial gas velocities is still poorly understood.

As pointed by Simiano and Lakehal 2012, the large-scale events (the bubble plume and plume meandering) are not necessary part of turbulence but they are part of the fluctuation velocity components. Therefore, the time series of the liquid velocity and the gas hold-up were employed to identify and educe the development of coherent flow structures. The contribution of each event was determined by analyzing the cross-correlation coefficient map. These events produce important fluctuations in the axial liquid velocity and gas void fraction. The procedure yielded the averaged topology of the three-dimensional large-scale structure events and was visualized using iso-surfaces of the vorticity for different gas flow rates. The structures have spiral tube-shaped topology rotating along the column near the walls with a pair of counter-rotating cells sustained through the flow. This work indicates that LES with the present pattern recognition can provide deep insights into developments of dynamics large-scale flow structures in turbulent flow field in gas-liquid bubble columns.

2. Two fluid model and numerical setup

2.1. The flow equations

The two-fluid model is based on the spatial filtering for LES or conditional averaging for RANS of the conservation equations of mass and momentum, where both phases, the continuous liquid phase

and the dispersed gas phases, are modelled as two interpenetrating continua, see Ishii and Hibiki 2006. The filtered equations are used to compute the large-scale lengths while the unresolved turbulent scales are modelled using a sub-grid model.

The present formulation closely follows the procedure outlined by Weller et al. 1998 and Weller 2005, where the mass and momentum equations for the phase φ are given by

$$\frac{\partial(\rho_\varphi \alpha_\varphi)}{\partial t} + \nabla \cdot (\rho_\varphi \alpha_\varphi \mathbf{U}_\varphi) = 0 \tag{1}$$

$$\frac{\partial(\rho_\varphi \alpha_\varphi \mathbf{U}_\varphi)}{\partial t} + \nabla \cdot (\rho_\varphi \alpha_\varphi \mathbf{U}_\varphi \mathbf{U}_\varphi) = -\alpha_\varphi \nabla p_\varphi + \alpha_\varphi \rho_\varphi \mathbf{g} - \nabla \cdot (\alpha_\varphi \rho_\varphi \boldsymbol{\tau}_\varphi^{\text{eff}}) + \mathbf{M}_\varphi \tag{2}$$

Here α_φ is the volume fraction of each phase, $\mathbf{U}_\varphi$ is the phase grid-scale velocity, and $\tau_\varphi^{\text{eff}}$ represents the combined mean viscous stress and turbulent stress tensor of phase φ

$$\boldsymbol{\tau}_\varphi^{\text{eff}} = -\nu_\varphi^{\text{eff}} \left[\nabla \mathbf{U}_\varphi + (\nabla \mathbf{U}_\varphi)^T - \frac{2}{3}(\nabla \cdot \mathbf{U}_\varphi)\mathbf{I} \right] + \frac{2}{3} k_\varphi \mathbf{I} \tag{3}$$

where k_φ is the turbulent kinetic energy of phase φ, $\mathbf{I}$ is the identity tensor, and ν_φ^{eff} is the effective viscosity of phase φ. The effective viscosity of the liquid phase is the sum of the molecular viscosity and the sub-grid viscosity

$$\nu_\varphi^{\text{eff}} = \nu_{L,\varphi} + \nu_{SGS} \tag{4}$$

and is formulated in the present study using the one-equation sub-grid-scale model by Niceno et al. 2008. The SGS model solves an additional transport equation for the unresolved kinetic energy k_{SGS}. The model of Niceno et al. 2008 accounts for effects of bubble induced turbulence through an additional source term in the transport equation for k_{SGS} in the continuous phase. The sub-grid kinetic energy equation reads

$$\frac{\partial k_{SGS}}{\partial t} + \nabla \cdot (k_{SGS}\mathbf{U}) - \nabla \cdot [(\nu + \nu_{SGS})\nabla k_{SGS}] = G - C_\varepsilon \frac{k_{SGS}^{3/2}}{\Delta} \tag{6}$$

where G is the production term, defined as follows

$$G = \nu_{SGS} |\bar{S}_{ij}| \tag{7}$$

and the sub-grid viscosity is

$$\nu_{SGS} = C_k \Delta k_{SGS}^{1/2} \tag{8}$$

The model constants are $C_\varepsilon = 1.05$ and $C_k = 0.07$, see Davidson 1997.

In Eq. (2), $\mathbf{M}_\varphi$ represents the inter-phase momentum exchange between phase φ and the other phase due to various interphase forces. In this study, the interfacial forces are decomposed into contributions from the drag, lift, virtual mass and turbulent drag which accounts for additional drag due to fluctuations in the dispersed phase. The total interfacial force acting between the two phases is given as

$$\mathbf{M}_\varphi = \mathbf{M}_\varphi^D + \mathbf{M}_\varphi^D + \mathbf{M}_\varphi^{VM} + \mathbf{M}_\varphi^{TD} \tag{9}$$

The terms on the right-hand side of Eq. (9) are

$$\mathbf{M}_\varphi^D = \frac{3}{4}\alpha_\varphi \rho_L \frac{C_D}{d_b} |\mathbf{U}_r| \mathbf{U}_r \tag{10}$$

$$\mathbf{M}_\varphi^L = \alpha_\varphi \rho_L C_L \mathbf{U}_r \times (\nabla \times \mathbf{U}_r) \tag{11}$$

$$\mathbf{M}_\varphi^{VM} = \alpha_\varphi \rho_L C_{VM} \left(\frac{D\mathbf{U}_c}{Dt} - \frac{D\mathbf{U}_d}{Dt} \right) \tag{12}$$

$$\mathbf{M}_\varphi^{TD} = -C_{TD} \rho_L k_L \nabla \alpha_G \tag{13}$$

Here $\mathbf{U}_r = \mathbf{U}_L - \mathbf{U}_G$ is the relative velocity between the continuous and the dispersed phases. The interfacial coefficients C_D, C_L, C_{VM} and C_{TD} are the drag, lift, virtual mass, and turbulent dispersion coefficients, respectively, which must be obtained from empirical correlations or analytical models. There are many models for each of these forces or coefficients depending on their applicability, the flow regime and operating conditions as discussed by Joshi, 2001 and Vial and Stiriba, 2013. The SGS component of those forces will be neglected except in the turbulent dispersion force which can be estimated using the modelled SGS energy. The drag coefficient was determined according to Schiller-Neumann correlation, the added mass coefficient C_{VM} is fixed to 0.5. The lift force which has been found to reproduce the radial dispersion of bubbles, as already pointed out by several authors, is justified for single bubble but for bubble swarm the uncertainty still remains. It is found that the simulations without considering the lift force best matches the experimental data. The sub-grid-scale turbulent dispersion force is adopted for the coarser and medium meshes since the grid

sizes are relatively larger than the bubble size, see Lopez de Bertodano et al. 1994, Niceno et al. 2008 and Tabib et al. 2011.

2.2 Numerical simulation set-up

The numerical simulations were carried out in a cylindrical bubble column with uniform aeration. The bubble column reactor is the same as used by Vial et al. 2000 and Vial et al. 2001(a)-(b) in their experiments. The height of the column is $H = 2$ m, the diameter is $D = 0.10$ m, and the static liquid height is 1.5 m. The reactor is operated with the water and air as the continuous and dispersed phases, at room temperature and atmospheric pressure, respectively, at two large superficial gas velocities 6 cm/s and 8.4 cm/s corresponding to transition and heterogeneous flow regimes.

The numerical simulations were carried out with the open source CFD package OpenFOAM library (Weller et al. 1998 and OpenFOAM user guide). The governing equations of continuity and momentum as well as the transport equation for k_{SGS} are solved by the two-phase flow solver twoPhaseEulerFoam available in OpenFOAM 2.3.1. The solver is based on a finite volume formulation to discretise the model equations which has shown to be stable for transient calculations, see Weller 2005. The first-order bounded implicit Euler scheme is adopted for the time integration, the gradient terms are discretized with a linear interpolation, the first-order upwind scheme for convective terms, and the diffusive terms are interpolated with the Gauss linear orthogonal scheme. we employ the PIMPLE algorithm to solve the pressure-velocity coupling where the pressure equation is solved, and the predicted velocities are corrected by the pressure change. The preconditioned conjugate gradient (PCG) is used for solving the discretized pressure equation and the incomplete-Cholesky preconditioned bi-conjugate gradient (BICCG) is used for other set of linear equations. For a more detailed discussions of all steps mentioned above, see Rusche 2002, Selma et al. 2010, and Weller 2005. The gas distributor is treated as a uniform mass flow rate inlet calculated from superficial gas velocities for mass conservation with a gas volume fraction of 1.0. The pressure at the inlet is set to zeroGradient and specified by zero gradient. At the outlet, the pressure is specified as atmospheric pressure, and the gas hold up is set to inletOutlet where zero gradient for outflow and fixed value for backward flow. Along the walls, no-slip conditions were applied.

For the present Euler-Euler LES approach, we have to consider the resolution requirement of both LES and the Euler-Euler approach simultaneously in order to choose a satisfactory grid. For the Euler-Euler model, the cell size should be larger enough than the largest interphase details of dispersed phase. In LES, the mesh has to be fine to resolve as much of the flow field as possible.

According to Dhotre et al. 2013 and Zhang et al. 2008, a successful LES much have a filter width in the initial subrange region, and all scales of motion larger than that must be resolved on the numerical grid. They indicated that the bubble diameter must be smaller than the cell size. Milelli et al. 2001 reported a systematic posterior analysis of the ratio of the bubble diameter to cut-off filter size: $\Delta/d_B \geq 1.5$, that is the mesh size must be at least 50% larger than the bubble diameter for Eulerian-Eulerian simulations. In the present case, the computational mesh was generated using the Gmsh finite element mesh generator. In order to check that the computed results are grid-independent, four different grids with $d_B/\Delta = 0.75, 1.1, 1.4$ and 1.875, have been analyzed by stretching the computational cell size near the walls. The coarser and medium mesh satisfy the Milelli condition, while the fine mesh does not. Fig. 4 shows the comparison of the axial liquid velocity and the gas hold-up. All the meshes show very similar results. In this work, we have employed the medium mesh with a filter width $\Delta = 5$ mm ($\Delta/d_B = 1.1$) which quantitively seems to give better agreements and ensures a good compromise between the CPU time and accuracy at the column center and close near the walls.

Note that for comparison, Niceno et al. 2008 used the criterion $\Delta/d_B = 1.2$ and found no significant different with different meshes, and the coarser one satisfying Milelli condition give a better agreement, Dhotre et al. 2008 found good agreement with experimental data using both conditions $\Delta/d_B = 1.2$ and $\Delta/d_B = 2.5$, and Liu et al. 2018 used the criterion $\Delta/d_B \leq 1.0$ and concluded that the grid size doesn't have to be larger than a single bubble size.

All transient calculations are started from static conditions with the liquid at rest and the gas is injected with a mass flow rate corresponding to the experimental superficial gas velocity. The bubble diameter is kept constant at 4 mm according to the experiments of Vial et al. 2001. Bubble coalescence and breakup are not considered in this work. We start with a fixed small-time step of $\Delta t = 0.0005$ s for the first 20 s then we increase it to 0.001 s in order to account for the transient instabilities of bubbly turbulent flows and satisfy the CFL condition $Co = \Delta t|\mathbf{U}|/\Delta x < 1$, where $|\mathbf{U}|$ is the magnitude of the velocity through a computational cell and Δx is the cell size in the direction of the velocity. The flow was simulated for 200 s and the averaged results from t = 50 s to t = 200 s are quantitively compared with experimental data. All the simulations were performed in parallel mode on a PC cluster with 16 nodes, Intel Xeon, 2.8 GHz, 4GH RAM.

3. Data processing and conditional sampling

LES and DNS methods provide fluid dynamics with data bases that use extended time series to give more details about the high intensity turbulent flows. Different methods to analyze those larger

data efficiently and identify coherent structures were developed. For instance, the proper orthogonal decomposition (POD), the dynamic mode decomposition (DMD), the coherent structure simulation (CVS), the fuzzy clustering technique, or the pattern recognition technique (PR). The second author gave a summary of different techniques used by different authors in references Usera et al. 2006 and Vernet et al. 1999.

The conditional sampling of the imprints on the plane of symmetry due to large flow structures, responsible of the circulation flow pattern in the bubble column, is performed by recording when the flow was statistically fully developed the time evolution of the instantaneous liquid velocity and gas hold-up in the computational domain during 0.5 s. The large-scale events (the bubble plume and plume meandering) are not necessary part of turbulence but they are part of the fluctuation velocity components (Simiano and Lakehal 2012). Therefore, time series of the liquid velocity and gas hold-up are needed to detect the flow structures responsible of their extreme values. The conditional sampling involves cross-correlating an initial template $\mathbf{U}_L(\mathbf{x},t)$ with the liquid velocity data $\mathbf{U}_L(\mathbf{x},t+\tau)$ sampled during the simulation. The cross-correlation is given by

$$R(\tau) = \frac{\overline{\mathbf{U}_L(\mathbf{x},t)\,\mathbf{U}_L(\mathbf{x},t+\tau)}}{\overline{\mathbf{U}_L(\mathbf{x},t)^2}} \tag{14}$$

The overbar indicates an average over $\mathbf{x}$ and t.

The conditional pattern recognition technique used is based on the detection of extrema values of the correlation coefficients in the plane of symmetry of the column. Fig. 3 shows the main steps of the conditional sampling technique procedure. As indicated in step 2 of Fig. 3, the cross-correlation coefficients of an initial template of the liquid velocity are stored in a three-dimensional matrix (i.e., two-dimensional matrix for each time step). The different templates used to detect the coherent structures consists of different multiple circulation cells and their selection will be discussed in the next section. Values of the cross-correlation coefficient larger than a threshold level (selected here to be the 1.5 times the *rms* value of the cross-correlation) identify the occurrence of individual events similar to the template. These events are ensemble averaged with the current ensemble average being used as the template for the next iteration. This procedure is repeated until the new template (i.e. ensemble average) is equal to the penultimate template. The time evolution of the spatial distribution of the liquid velocity produces that regions where the maximum of the correlation coefficient appears. The positions and the time at which the selected events occur are stored in a file, and then we use this information to obtain the conditional ensemble averaging of the flow at the plane of symmetry in the reactor.

The regions where the maxima of the correlation coefficients occur are selected as elongated volumes since the extreme values move along the streamwise and spanwise directions. In these volumes, only region of the plane corresponding to time where the absolute maximum of the correlation occurs is chosen to obtain the ensemble average of the liquid velocity event. In this way, the procedure will prevent selecting different stages of the same event at different times. The present technique resembles that applied by Pallares et al. 2010 in natural convection vertical channel flow. Similar pattern recognition procedure was used by Vernet et al. 1999 to analyze three-dimensional structures in a turbulent cylinder weak. The information obtained is employed to calculate the vorticity when and where the selected event occurs.

4. Results and discussions

Fig. 5 and 6 show a comparison between numerical simulations using both the $k-\varepsilon$ model and the LES against experimental measurement of Vial et al. 2001 for the mean axial liquid profile and axial fluctuating liquid velocity, respectively. It can be seen that the models capture experimental data reasonably well in both flow transition regime ($U_G = 6$ cm/s) and heterogenous flow regime ($U_G =$ 8.4 cm/s). In the core region, $x/R \leq 0.9$, both models give nearly the same results. For the initial superficial gas velocity $U_G = 6$ cm/s, the Euler-Euler LES approach gives a better agreement with experimental data both in the core region and close near the wall. In Fig. 6 we display the time averaged *rms* axial liquid velocity calculated by LES and RANS model. We can see clearly that LES performs better than RANS. Unfortunately, experimental data on kinetic turbulent energy of the liquid phase are not available. In fact, Vial et al. 2001 only measured the *rms* in the axial and orthoradial directions. For $U_G = 8.4$ cm/s, however, the liquid velocity is overpredicted at high superficial gas velocity between the central plume region and the vortical flow region. The reason of this deviation as the performance of LES with respect to RANS are not clarified and may be attributed to the single bubble size distribution of 4 mm using in our two-phase flow model and the interfacial forces employed. In this region the flow is characterized by cluster of bubbles at relatively low velocities and coalesced bubbles moving at high velocities, see Chen et al. 1994. Furthermore, we found that the RANS model performs better with inclusion of the turbulent dispersion force which spreads the bubble plume. While the trend in LES calculations is to neglect the unresolved sub-grid scale, we found that such interfacial sub-grid-scale force improves the liquid velocity profile as Tabib et al. 2011 who quantified the SGS-TDT and found that, for the bubble column reactor, its magnitude is small as compared to the momentum advection, the drag and resolved turbulent dispersion forces. They pointed the need of research works towards finding suitable SGS-TD force model.

Note that for comparison, Zhang et al. 2008, simulated different bubble column reactors with different aspect ratios employing a sub-grid scale model and the $k-\varepsilon$ model and different interfacial closure correlations. They found that both models can produce a good solution for the time-averaged vertical velocity and there is not yet a universal interfacial closure model available for the simulation of the bubble column flow.

Typical time series of the axial liquid velocity components at height of 0.7 m are depicted in Fig. 7 and show the transient behavior and statistically stationary with constant mean velocity. The energy spectrum density obtained from LES calculations is shown in Fig. 8. It can be seen the classical -5/3 law holds at the initial superficial gas velocity of $U_G = 8.4$ cm/s and deviates slightly at $U_G = 6$ cm/s in the initial subrange. Previous experimental and numerical studies attributed this fast decay and the more dissipative spectrum to buoyancy-generated inertia forces and the bubble-induced viscosity effects, see Dhotre et al. 2008 and Lance and Bataille 1991. Both spectra consist on numerous dominant peaks in the 0-120 Hz frequency band and exhibit several peaks, for example 15 and 35 Hz at $U_G = 8.4$ cm/s and 40 and 60 Hz at $U_G = 6$ cm/s which indicate the transient behavior of the system. Indeed, the low frequencies are never observed. Both flow regimes are characterized by existence of liquid flow circulation pattern and thus macro-structures in both phases that move alternatively upwards and downwards as observed numerically in this work and experimentally by several authors, see Vial et al. 2001 and Olmos et al. 2003. This corresponds to quasi-periodic phenomena that induces high velocities fluctuations and new frequencies.

In Fig. 9, the time-averaged and selected instantaneous snapshots of liquid velocity fields with the corresponding gas hold-up are displayed at times 60, 70 and 80 s, respectively. The LES resolves the flow with much more details as reported by Deen et al. 2001 and Dhotre et al. 2008. Large vortices can be observed in the column center and some circulations in the near-wall region. The flow pattern changes with time and large amount of the gas moves through the central plume region and deviates from the flow characteristics obtained by time-averaging. As can be seen a bubble plume structure starts from the distributor zone up to the free surface and becomes much pronounced with high inlet gas flow rate. Several liquid circulation cells are continuously generated and convected throughout the column height. Their number and size are changes with time and the inlet superficial gas velocity. The same vortices were observed by Chen el al. 2004 through flow visualization using laser sheeting and PIV system for the gas velocity between 2.1 and 4.2 cm/s. They found the general flow pattern displayed in Fig. 1(a). They reported existence of different large flow structures under different flow regimes, see for example Fig. 1(b). For the vortical-spiral flow regime, clusters of bubbles form in the central bubble stream moving in a spiral manner with the liquid moving spiraling downward close

to the wall column, see Fig. 1. Here we observe the existence of four instantaneous regions. Joshi et al. 2002 pointed out existence low-frequency circulation cells in both 2D and 3D bubble column reactors and the potential of LES to simulate and explore the coherent structures. The onset, size, location and numbers of the circulation cells change instantaneously in the column.

By combining the information from the above discussion with visual observations on instantaneous liquid circulation patterns depicted in Fig. 9, a pair of nonsymmetric circulation cells were identified and have been used as the initial templates to analyze the liquid velocity field recorded simultaneously with the gas hold-up and to detect where correlation coefficient attains extreme values, see Fig. 10. It consists of two staggered lobes of different positions observed at the plane of symmetry of the bubble column. Fig. 11 displays the autocorrelation function of axial liquid velocity at mid height of the column reactor for $U_G = 6$ cm/s and 8.4 cm/s, respectively. In both cases, the correlation coefficients present an exponentially decreasing shape and go to 0 for a delay of 5 s and then it starts to fluctuate above and beyond 0. Time evolution of 450 individual samples of the liquid velocity and gas hold-up at the plane of symmetry during a period of 200 s were used to educe the flow structures.

The number and position in the axial direction where the maximum of the correlation coefficient between the template and the detected event occurs are displayed in Fig. 12. At superficial gas velocity $U_G = 6$ cm/s, an average of 79 and 66 events were selected for templates 1 and 2, respectively, with a correlation coefficient of 0.65. The flow structure of both templates is characterized by a fast bubble flow region including cluster of bubbles moving in a wavy spiral motion through the column with gross scale liquid circulation carried upward in the bubble stream and downward motions of liquid pockets in the vortical spiral flow region which still may include bubbles. This structure corresponds to churn-turbulent flow regime and was obtained experimentally through the PIV techniques in other 2D and 3D bubble column reactors by other authors. One can see that those macroscopic structures appear near the sparger and at different heights between 0.2 and 1 m. At superficial gas velocity $U_G = 8.4$ cm/s, the flow regime turns from vortical-spiral to turbulent and an average of 79 and 82 events were selected for templates 1 and 2, respectively, with a correlation coefficient of 0.65. The bubble velocities and turbulence intensity are enhanced along the column in both the fast bubble and the central plume regions and the vortexes are more stretched. Note that the structure number in this flow regime is much higher close to the sparger zone than in the spiral-vortical region. By comparing different pictures one can see that the two structures can occur simultaneously in more than 60 % but at different locations and then disappear near the free surface.

The conditionally ensemble averaged instantaneous liquid velocity components, gas hold-up and velocity field constructed with axial and streamwise liquid velocity components are shown in Fig 13 and 15. The weakness of (u, v) velocity field in comparison with the contribution of the axial velocity can be assessed. The streamwise velocity attains its maximum/minimum between the vortices and is symmetric in the selected plane, whereas the spanwise component corresponding to template 1 exhibits a minimum at the center of one circulation which nearly balanced by that at the other opposite circulation, that is, only v changes the sign. For the vortical structures of template 2, the v −velocity attains its maximum in each vortex. These changes of sign lead to movement of the vortical structure back and forth. Fig. 13(d) and Fig. 15(d) show the liquid flow fields with velocity vectors and contours of gas hold-up. The gas void fraction has the same trend as the axial liquid velocity. The liquid flow is accelerated where more bubbles are located and decelerated with less bubbles. The bubbles are accumulated at the center of the plane and rise back or forth since the streamwise liquid velocity is very small.

In Fig. 14 we display the ensemble average of the fluctuation values. The magnitude of velocity fluctuations w' are higher than u' and v' which explain the anisotropy of the turbulence. The fluctuations of the axial velocity and gas hold-up peak at each cell vortex whereas u' peaks in the center. The nature of the fluctuations can be explained by the fact that the vortical structure move upward at the central part of the column and upward and downward close to the walls. The flow in this region experiences small fluctuations in the spanwise component of the liquid velocity leading v' to peak along the walls. The LES model predicts non-zero streamwise fluctuating velocities only at the center region of the column which accelerates the flow and force the bubble plume to meander only in this region. The trend of the void fraction fluctuations resembles that of the axial velocity fluctuations. It is clear that the bubbles induce a substantial turbulence both in central plume and fast bubble regions which gets stronger with increasing α_G' and show a peak in the vortical spiral region.

To further analyze the conditionally averaged flow structure responsible for the large vortical structures we use the vorticity vector calculated from instantaneous liquid velocity

$$\omega_x = \frac{\partial w}{\partial y} - \frac{\partial v}{\partial z}, \qquad \omega_y = \frac{\partial u}{\partial z} - \frac{\partial w}{\partial x}, \qquad \omega_z = \frac{\partial v}{\partial x} - \frac{\partial u}{\partial y}$$

and the magnitude $|\omega| = \left(\omega_x^2 + \omega_y^2 + \omega_z^2\right)^{1/2}$. A quantity used by Jeong and Hussain 1995 to detect the vortex cores and represent their topology and also by Simiano and Lakehal 2012 to analyze the mean flow filed in the bubble plume. The vorticity provides insights on the oscillatory behavior of the plume. Fig. 16(a)-(b) and 17(a)-(b) depict the lateral vorticity ω_y at the symmetry plane of the

column and streamlines. The vorticity shows a complex radial distribution with elevation: in the core region ($0.04\text{m} \leq x \leq 0.06$ m), encompassing both the central plume and fast bubble region, ω_y is dominated by both $\partial u/\partial z$ and $\partial w/\partial x$ which reflects a flow retraction features to be discussed in the context of Fig. 15, and only by $\partial w/\partial x$ (i.e., $\omega_y \approx -\partial w/\partial x$) in the vortical-spiral region (0.07 m $\leq x \leq 0.1$ m) which promote flow acceleration in the axial direction close to the walls, see Fig. 13. In fact, in the central plume region $\partial u/\partial z$ exhibits strong drop while $\partial w/\partial x$ remains small in some parts, and toward the walls $\partial w/\partial x$ has strong jumps meantime the streamwise velocity is very small. The rising bubbles have a two-dimensional zig-zag motion. It shows two lobes in the central plume region with inclined double roller structure and other two lobes in the vortical spiral flow region close to the walls. The vorticity magnitude is nearly equal in each lobe and the highest level occurs at the lower spanwise eddy. The focus of the primary vortices is located between the fast bubble region and the central plume region while the focus of the secondary vortices is shifted from the vortical spiral region to near wall by strong bubble backflow.

Three-dimensional plot of $|\omega|$ iso-contours are displayed in Fig. 16(c) and 17(c), the flow structure has spiral tube-shaped topology where swarm of bubbles rises along 3D helical trajectories around within the central bubble plume region. The plume rotates along the axial direction near the walls and the sharp edge corresponds to the peak of vorticity shown in Fig. 16(a)-(b) and Fig. 17(a)-(b). The flow structure responsible for liquid circulation convects the flow from the fast bubble plume region toward the walls. It seems that it doesn't cross the column via the centerline with an irregular rotation. This irregular movement is continuous for $U_G = 6$ cm/s and becomes faster for $U_G = 8.4$ cm/s but the shifting of the plume structure could be considered to be continuous and similar in both cases. A pair of counter-rotating cells are sustained through the flow and move spirally upwards while the bubble plume changes position which are found experimentally to entrain small bubble. The width of the plume is comparable with the column diameter and seems to fill the entire column. The picture is a schematic representation of the flow structure in higher-aspect ratio bubble columns for both medium and high gas flow rate, as observed visually. The flow pattern displays a number of cells which move dynamically upward while the bubble plume changes position.

5. Conclusions

Database obtained from Euler-Euler large eddy simulations of the gas-liquid flow in a three-dimensional cylindrical bubble column has been analyzed to numerically investigate transient large flow structures associated with rising bubbles in a semi batch reactor. The sub-grid scale modeling is

based in the one-equation model and the bubble-induced turbulence was modelled by extra source terms added in the transport equation for SGS kinetic energy. The initial superficial gas velocity is taken so that the flow is in the churn-turbulent flow regimes.

The instantaneous results of LES reveal that the flow pattern is dominated by vortical structures. Multiple low-frequency cells of different sizes have been observed in the vortical-spiral flow region. The averaged large flow structures are educed using a conditional sampling technique and they consists in two counter-rotating vortices that move in a wavy-spiral motion through the column. The cross-correlation coefficient maps were obtained. For one template a nearly 79 events were detected in the spiral flow regime and 82 events in the turbulent regime with a correlation coefficient of 0.65. The two flow structures can occur simultaneously in more than 60 % but at different locations. The procedure yielded the topology of the three-dimensional large-scale structure which was visualized using iso-surfaces of the vorticity for different gas flow rates. The structures have spiral tube-shaped topology rotating along the column near the walls with a pair of counter-rotating cells sustained through the flow. The trend of bubble induced turbulence resembles that of the void fraction. This study provides analysis of instantaneous flow information and pattern recognition of air-water flow which are crucial in further understanding hydrodynamics and flow transition of multiphase flow in bubble column reactors.

Acknowledgements

This study was financially supported by the Spanish Ministry of Economy, Industry and Competitiveness – Research National Agency under project DPI2016-75791-C2-1-P, FEDER funds and by Generalitat de Catalunya – AGAUR under project 2017 SGR 01234.

References

1 Bauer, M., Eigenberger, G., 1999. A Concept for Multi-scale Modelling of Bubble Columns and Loop Reactors. Chem. Eng. Sci. 54, 5109–5118.

2 Chen, R.C., Reese, J., Fan, L.-S., 1994. Flow structure in a three-dimensional bubble column and three-phase fluidized bed. AIChE J. 40, 1093-1104.

3 Deen, N.G., Solberg, T., Hjertager, B.H., 2001. Large eddy simulation of the gas-liquid flow in a square cross-sectioned bubble column. Chem. Eng. Sci. 56, 6341-6349.

4 Dhorte, M.T., Niceno, B., Smith, B.L., Simiano, M., 2009. Large eddy simulation (LES) of large-scale bubble plume. Chem. Eng. J. 64, 2692-2704.

5 K. Ekambara, M.T. Dhorte, 2010. CFD simulations of bubble column. Nuc. Eng. Des. 240, 963-969.

6 Harteveld, W.K., Mudde, R.F., Groen, J.S., Van Den Akker, H.E.A., 2003. Dynamics of bubble columns: Influence of gas distribution and coherent structures. Canadian J. Chem. Eng. 81, 389-394.

7 Harry Van Den Akker, E.A., 1998. Coherent structures in multiphase flows. Powder Tech. 100, 123-136.

8 Ishii, M., Hibiki, T., 2006. Thermo-fluid dynamics of two-phase flow, 2nd edition. Springer, New York, 2006.

9 Jakobsen, H.A., Lindborg, H., Dorao, C.A., 2005. Modelling of bubble column reactors: Progress and limitations. Ind. Eng. Chem. Res. 14, 5107-5151.

10 Jamialahmadi, M., Müller-Steinhagen, H., 1989. Bubble formation and coalescence in bubble columns. Chemie Ingenieur Tech. 61, 715-718.

11 Jeong, J., Hussain, F., 1995. On the identification of a vortex. J. Fluid Mech. 285, 69-80.

12 Joshi, J.B., Sharma, M.M., 1979. A circulation cell model for bubble columns. Trans. of the Inst. of Chem. Eng. Sci., 57, 244-251.

13 Joshi, J.B., 1980. Axial mixing in multiphase contactors – a unified correlation. Trans. of the Inst. of Chem. Eng. Sci., 58, 155-165.

14 Joshi, J.B., 2001. Computational flow modelling and design of bubble column reactors. Chem. Eng. Sci., 56, 5893-5933.

15 Joshi, J.B., Vitankar, V.S., Kulkarani, A.A., Dhorte, M.T., Ekambara, K., 2002. Coherent structures in bubble column reactors. Chem. Eng. Sci. 57, 3157-3183.

16 Lin, T.-J., Reese, J., Hong, T., Fan, L.-S., 1996. Quantitative analysis and computation of two-dimensional bubble columns. AIChE J. 42, 301-318.

17 Lance, M., Bataille, J., 1991. Turbulence in the liquid phase of a uniform bubbly air-water. J. Fluid Mech. 222, 95-118.

18 Lapin, A., Lübbert, A., 1994. Numerical Simulation of the Dynamics of Two-phase Gas-liquid Flows in Bubble Columns. Chem. Eng. Sci. 49, 3661–3674.

19 Liu, Z., Li, B., 2018. Scale-adaptive of Euler-Euler large eddy simulation for laboratory scale dispersed bubbly flows. Chem. Eng. J. 338, 465-477.

20 Masood, R.M.A., Delgado, A., 2014. Numerical investigation of the interphase forces and turbulence closure in 3D bubble column. Chem. Eng. Sci. 108, 154-168.

21 Milelli, M., 2002. A numerical analysis of confined turbulent bubble plume. Diss. EH. No. 14799, Swiss Federal Institute of Technology, Zurich, 2007.

22 Mudde, R.F., 2005. Bubbly gravity-driven flows. Annu. Review. Fluid. Mech. 37, 393-423.

23 Mudde, R.F., Groen, J.S., Van Den Akker, H.E.A., 1997. Liquid velocity field in a bubble column: LDA experiments. Chem. Eng. Sci. 52, 4217-4224.

24 Mudde, R.F., Groen, J.S., Van Den Akker, H.E.A., 2002. Coherent structures and axial dispersion in bubble column reactors. Chem. Eng. Sci. 51, 2511-2520.

25 Mudde, R.F., Simonin, O., 1999. Two- and three-dimensional simulations of a bubble plume using a two-fluid model. Chem. Eng. Sci. 54, 5061-5069.

26 Olmos, E., Gentric, C., Vial, Ch., Wild, Midoux, N., 2001. Numerical simulation of multiphase flow in bubble column reactors. Influence of bubble coalescence and break-up. Chem. Eng. Sc. 56, 6389-6365.

27 Olmos, E., Gentric, C., Vial, Ch., Wild, Midoux, N., 2003. Description of flow transitions in bubble column via laser Doppler anemometry signals processing. Chem. Eng. Sc. 58, 1731-1742

28 OpenFOAM Ltd., United Kingdom, 2012, OpenFOAM 2.1.1 user's guide.

29 Pallares, J., Vernet, A., Ferre, J.A., Grau, F.X., 2010. Turbulent large-scale structures in natural convection vertical channel. Int. J. Heat Mass Transf. 53, 4168-4175.

30 Rusche, H., 2002. Computational fluid dynamics of dispersed two-phase flows at high phase fractions. Ph.D. Thesis, Imperial College, University of London.

31 Sathe, M.J., Mathpati, C.S., Deshpande, S.S., Khan, Z., Ekambara, K., Joshi, J.B., 2011. Investigation of flow structures and transport phenomena in bubble columns using particle image velocimetry and miniature pressure sensors. Chem. Eng. Sci. 66, 3087-3107.

32 B. Selma, B., R. Bannari, R., P. Proulx, P., 2010. A full integration of a dispersed and interface closures in the standard model of turbulence. Chem. Eng. Sci. 65, 5417-5428.

33 Sokolichin, A., Eigenberger, G., Lapin, A., 2004. Simulation of buoyancy driven bubbly flow: Established simplifications and open questions. AIChE J. 50, 24–45.

34 Simiano, M., Lakehal, D., 2012. Turbulent exchange mechanisms in bubble plumes. Int. J. Multiphase Flows. 47, 141-149.

35 Stiriba, Y., Gourich, B., Vial, Ch., 2017. Numerical modelling of ferrous iron oxidation in a split-rectangular airlift reactor. Chem. Eng. Sci. 170, 705-719.

36 Sun, J., Wang, J., Yang, Y., 2012. CFD simulation and wavelet transform analysis of vortex and coherent structure in a gas-solid fluidized bed. Chem. Eng. Sci. 71, 507-519.

37 Tabib, M.V., Schwarz, P., 2011. Quantifying sub-grid (SGS) turbulent dispersion force and its effect using one-equation SGS large eddy simulation (LES) model in a gas-liquid and a liquid-liquid system. Chem. Eng. Sci. 68, 3071-3086.

38 Tzeng, J.-W., Chen, R.C., Fan, L.-S., 1993. Visualization of flow characteristics in a 2-D bubble columns and three-dimensional fluidized bed. AIChE J. 39, 733-744.

39 Usera, G., Vernet, A., Pallares, J., Ferré, J, 2006. A conditional sampling method based on sampling based on fussy clustering for the analysis of large-scale dynamics in turbulent flows. European J. Fluid Mech., 25, 172-191.

40 Vernet, A., Kopp, G.A., Ferré, J.A., Giralt, F., 1999. Three-dimensional structure and momentum transfer in a turbulent cylinder wake. J. Fluid Mech. 394, 303-337.

41 Vial, Ch., Camarasa, E., Poncin, S., Wild, G., Midoux, N., Bouillard, J., 2000. Influence of gas distribution and regime transition on liquid velocity and turbulence in a bubble column. Chem. Eng. Sci. 55, 2957-2973.

42 Vial, Ch., Lainé, R., Poncin, S., Midoux, N., Wild, G., 2001(a). Influence of gas distribution and regime transition on liquid velocity and turbulence in a bubble column. Chem. Eng. Sci. 56, 1085-1093.

43 Vial, Ch., Poncin, S., Wild, G., Midoux, N., 2001(b). A simple method for regime identification and flow characterization in bubble columns and airlift reactors. Chem. Eng. and Proc. 56, 135-151.

44 Vial, Ch., Stiriba, Y., 2013. Characterization of bioreactors using computational fluid dynamics. Fermentation Processes Engineering in the Food Industry, C.R. Soccol, A. Pandey, C. Larroche Eds. – Taylor & Francis Group – 978-1-4398-8765-3, 121–164.

45 Weller, H.G., 2005. Derivation, modelling and solution on the conditionally averaged two-phase flow equations. Technical Report TR/HGW/02, OpenCFD Ltd.

46 Weller, H.G., Tabor, G., Jasak, H., Fureby, C., 1998. A tensorial approach to computational continuum mechanics using object-oriented techniques. Comput. Phys. 12, 620-631.

47 Zehner, P., 1982. Momentum, mass and heat transfer in bubble columns. Intern. Chem. Eng. 26, 22-35.

48 Zhang, D., Deen, N.G., Kuipers, J.A.M., 2006. Numerical simulation of the dynamic flow behavior in a bubble column: a study of closures for turbulence and interface forces. Chem. Eng. Sci. 61, 7593-7608.

Mesh	$\Delta x \times \Delta y \times \Delta z$ $(\mathbf{mm^3})$	Δ / d_B
Mesh 1	$7.5 \times 7.5 \times 7.5$	1.875
Mesh 2	$5 \times 5 \times 7$	1.4
Mesh 3	$5 \times 5 \times 5$	1.1
Mesh 4	$3 \times 3 \times 3$	0.75

Table 1. The computational mesh and grid spacing investigated.

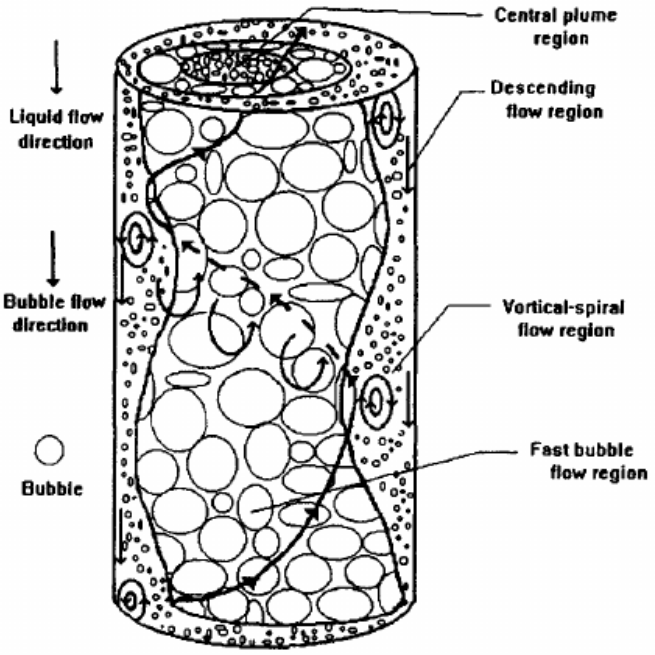

(a)

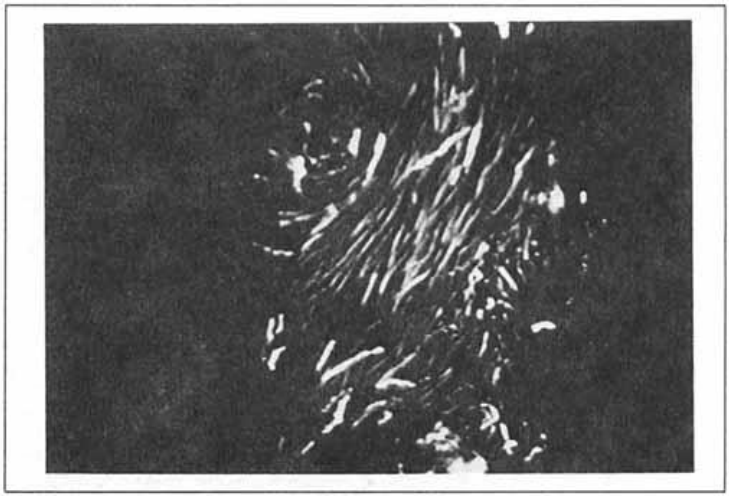

(b)

Fig. 1. (a) Instantaneous flow structure in a 3-D bubble column and (b) liquid flow field at $U_G =$ 3.3 cm/s. (Chen et al., 1994).

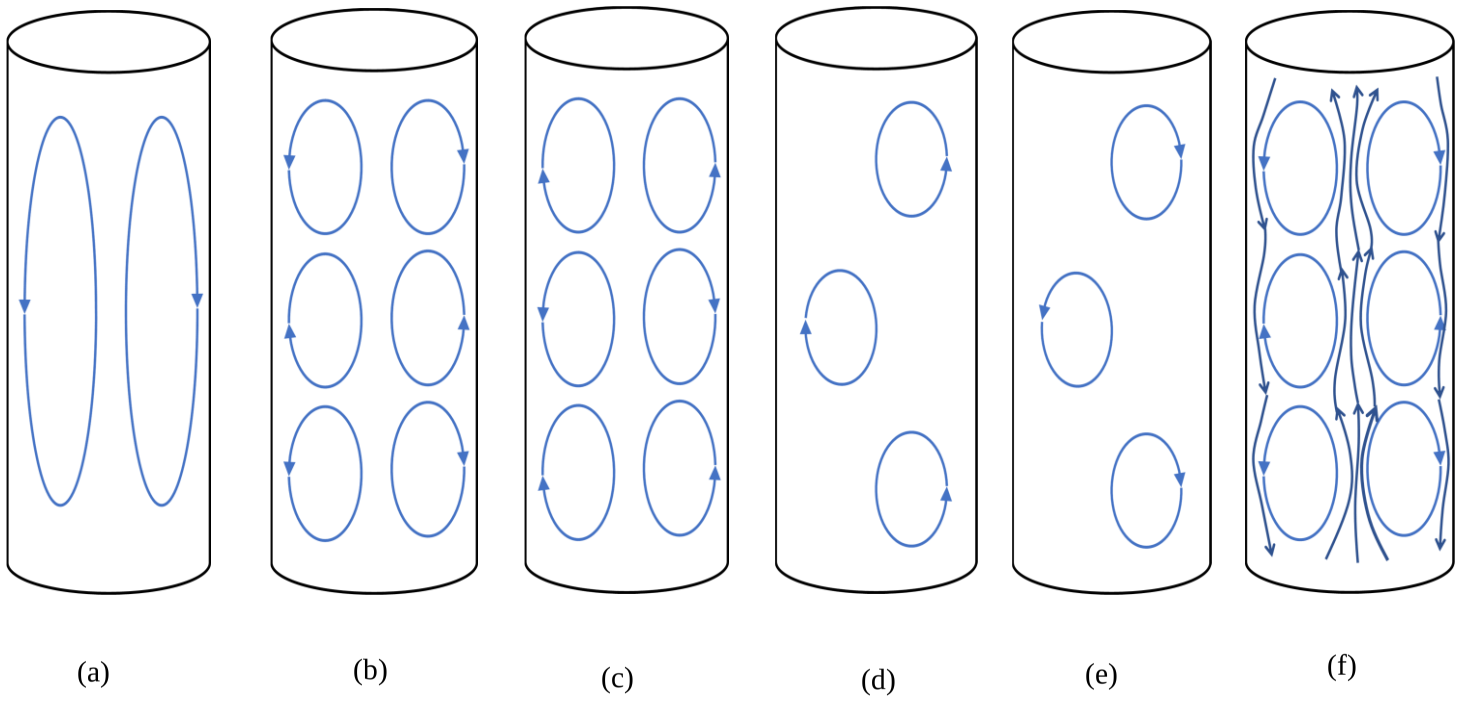

Fig. 2. Different liquid circulation cell structures in bubble column

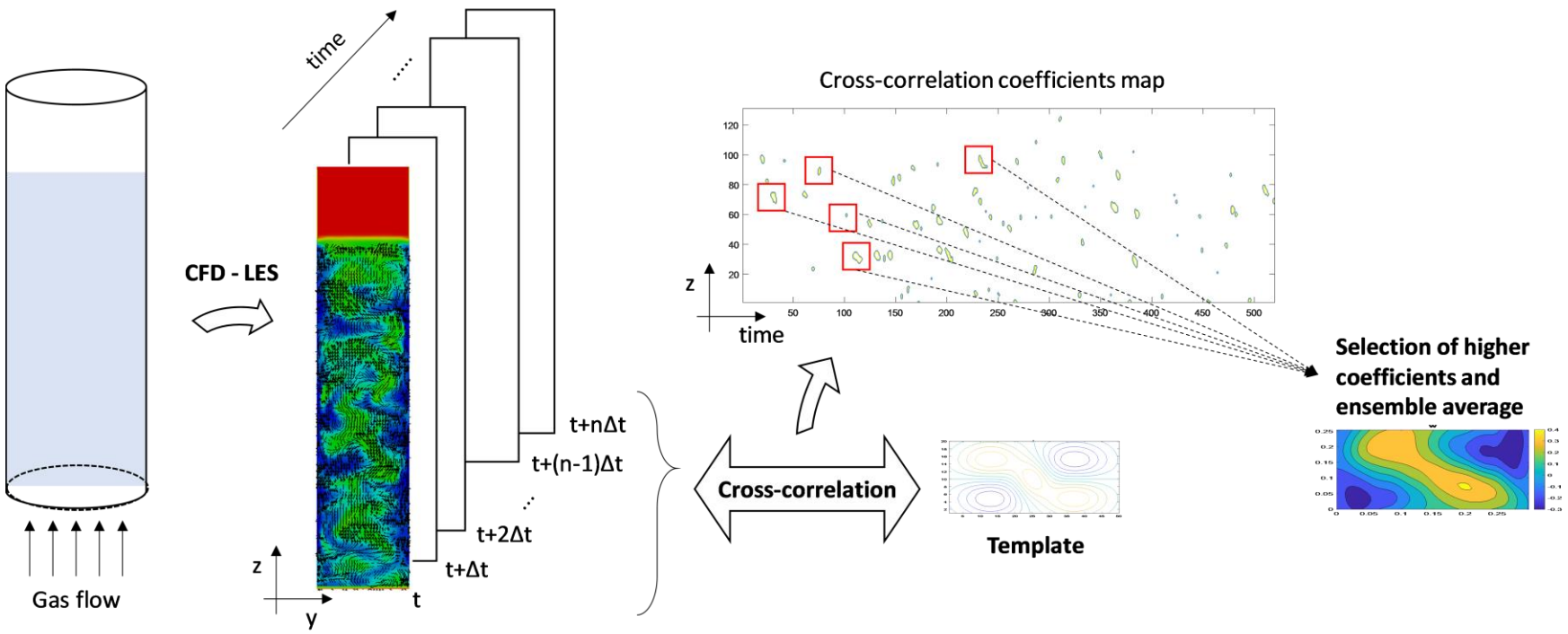

Fig. 3. The different steps of the conditional sampling procedure

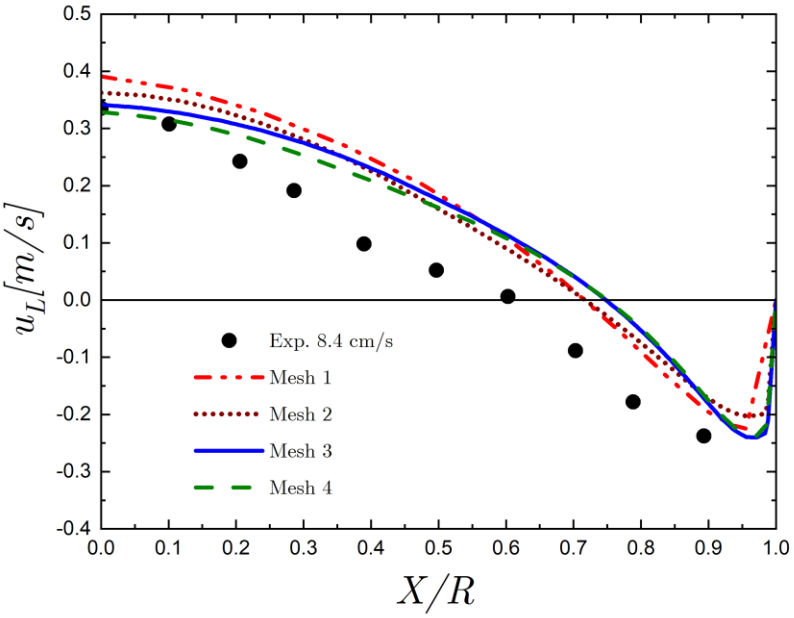

Fig. 4. Comparison of the time-averaged results for the axial liquid and the different meshes investigated at $U_G = 8.4$ cm/s.

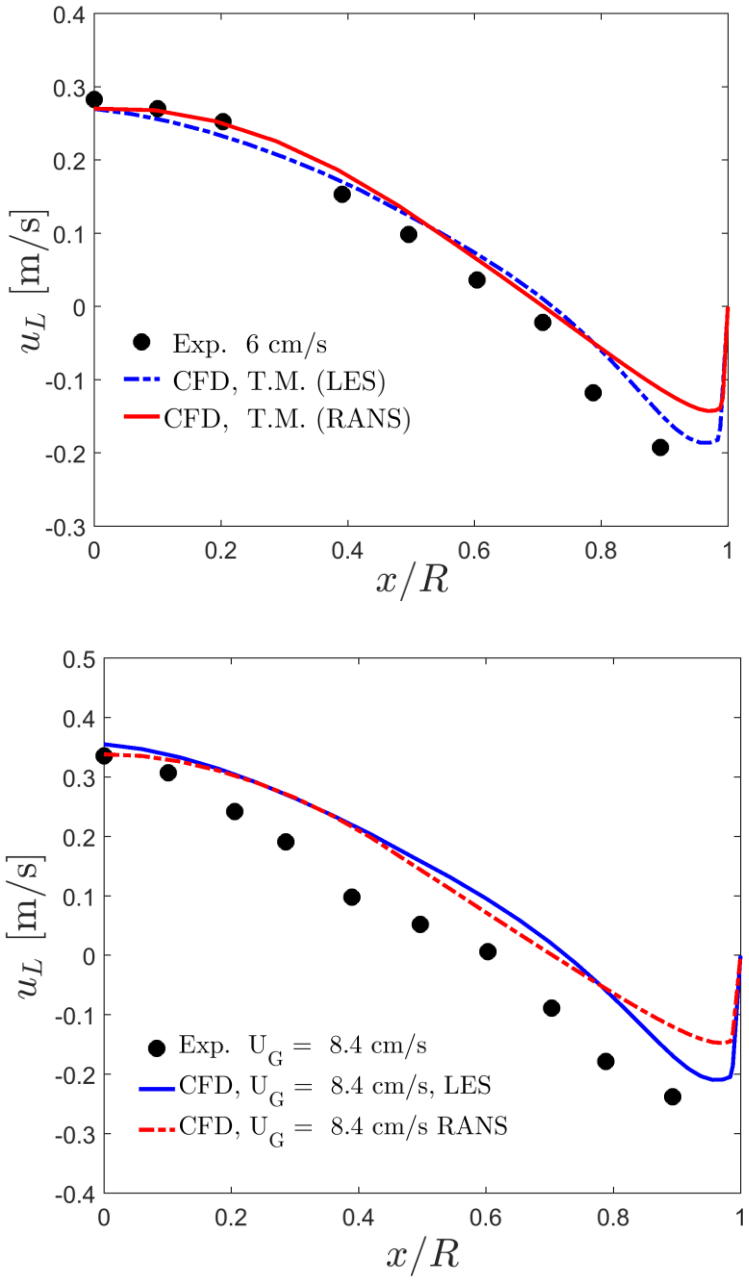

Fig. 5 Comparison of the calculated time averaged axial liquid velocity with experimental measurements at the height $h = 0.7$ m with mixture $k - \varepsilon$ and one-equation LES models.

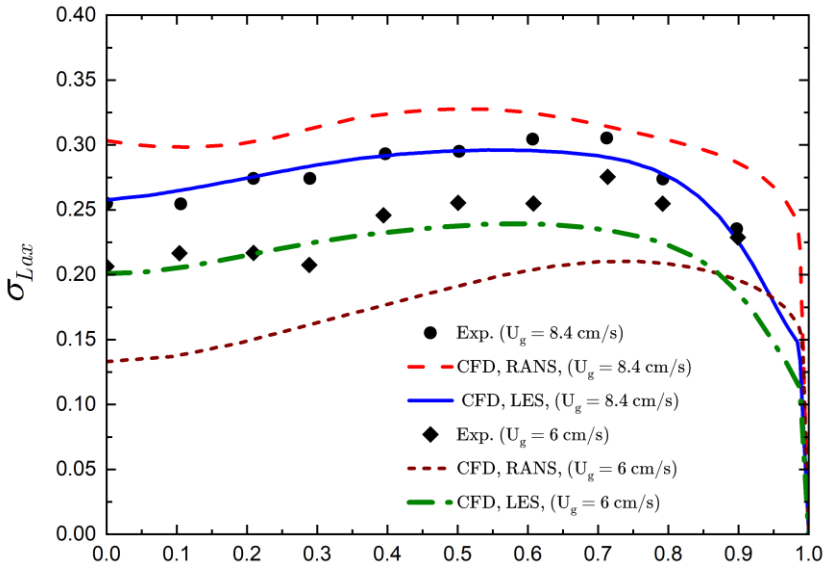

Fig. 6 Comparison of the calculated time averaged rms axial liquid velocity with experimental measurements at the height $h = 0.7$ m with mixture $k - \varepsilon$ and one-equation LES models.

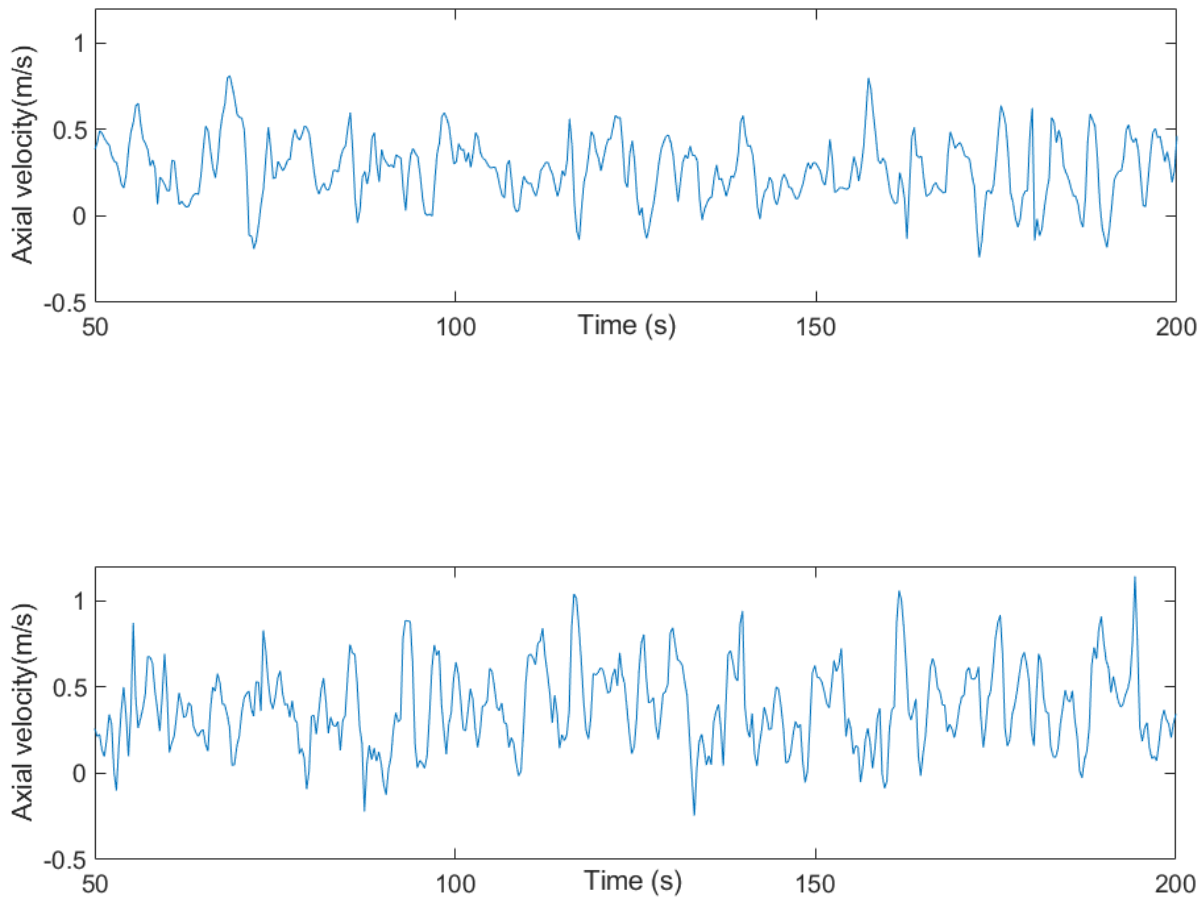

Fig. 7 Time history plots of the axial liquid velocity between $t = 50$ s and 200 s at $(0.05\text{ m}, 0.05\text{ m}, 0.7\text{ m})$ of the column at inlet superficial gas velocity $U_G = 6$ cm/s (top) and $U_G = 8.4$ cm/s (bottom).

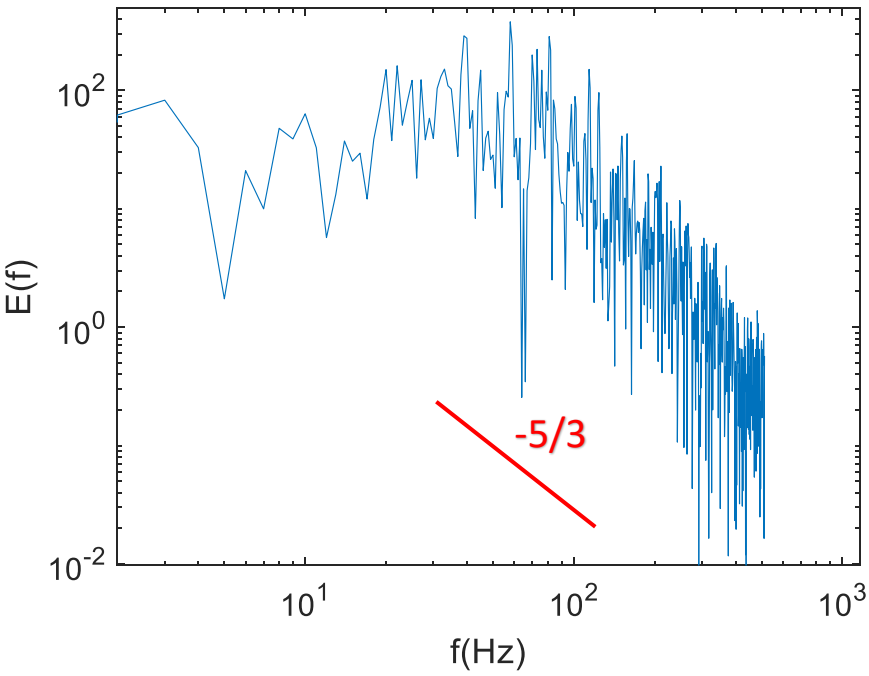
E(f)
10^2
10^0
10^{-2}
-5/3
10^1
10^2
10^3
f(Hz)

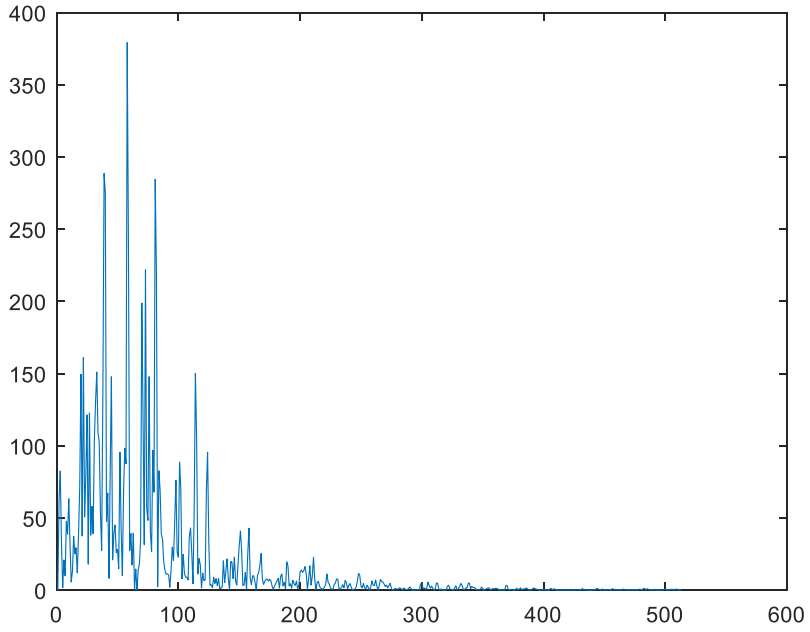
400
350
300
250
200
150
100
50
0
0
100
200
300
400
500
600

(a)

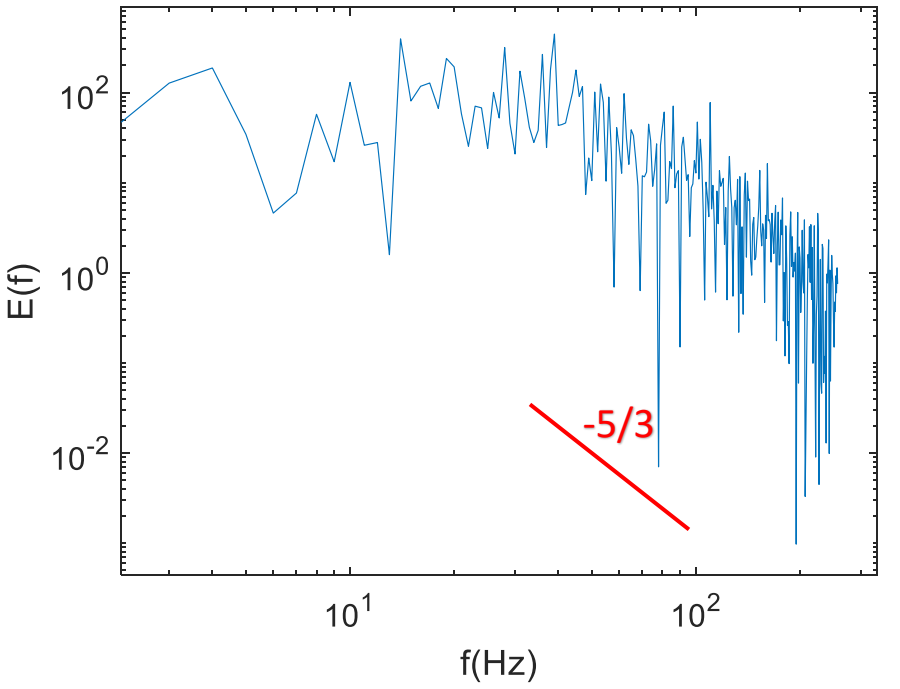

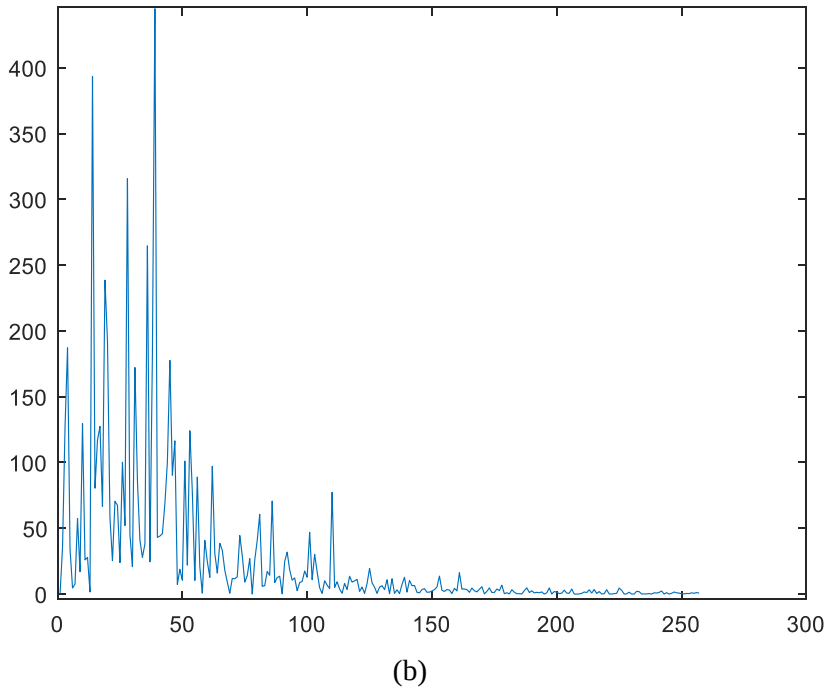

(b)

Fig. 8 Power spectra density of the axial liquid velocity at $(0.05\ \text{m}, 0.05\ \text{m}, 0.7\ \text{m})$ of the column at inlet superficial gas velocity $U_G = 6$ cm/s (a) and $U_G = 8.4$ cm/s (b).

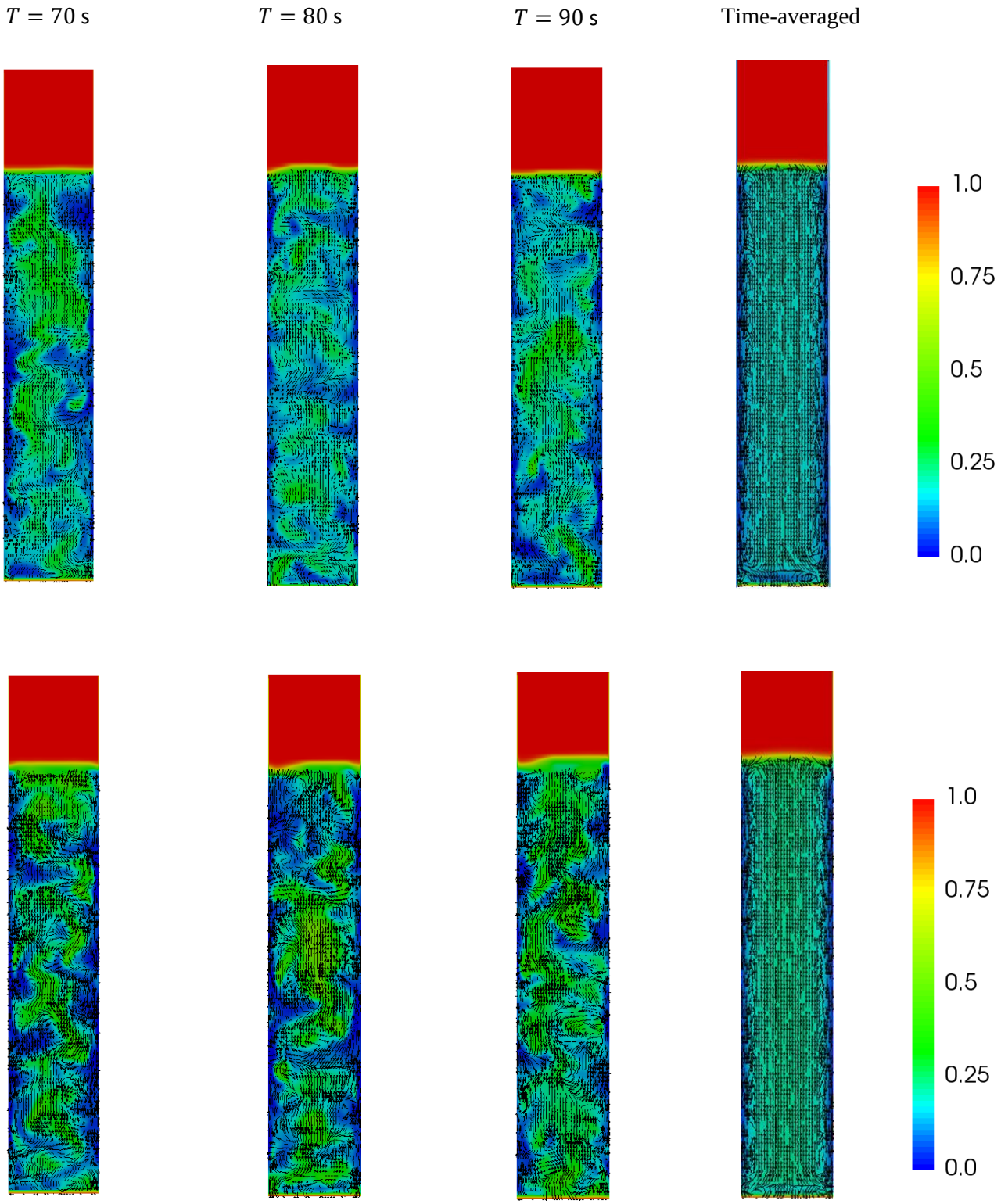

Fig. 9 Predicted instantaneous and time-averaged vector field for liquid velocity and gas hold-up at inlet superficial gas velocity $U_G = 6$ cm/s (top) and $U_G = 8.4$ cm/s (bottom).

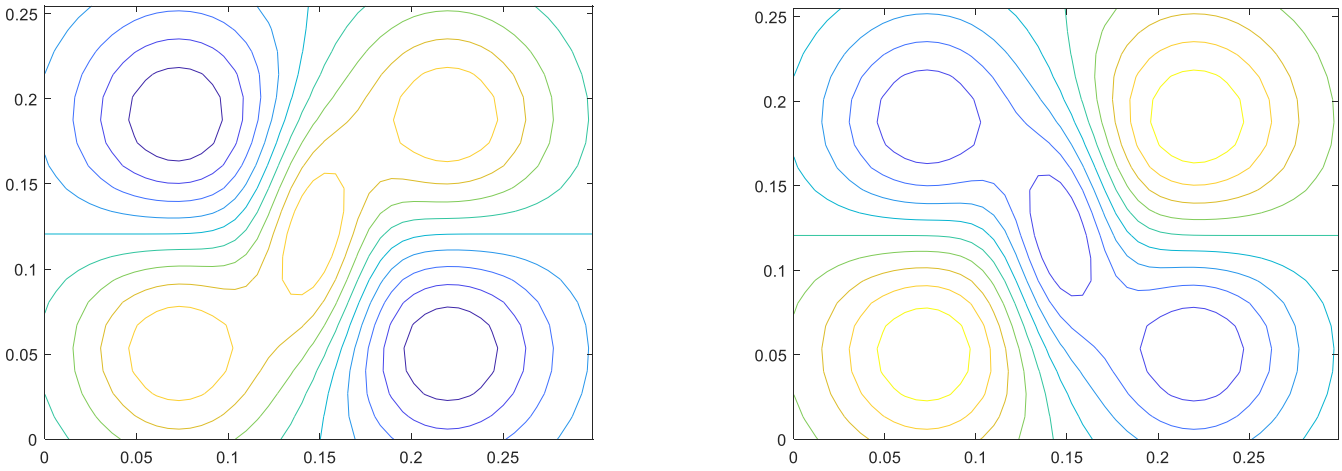

Fig. 10 Iso-contours of the initial templates depicting the cell circulations by the liquid velocity in the (x, z)-plane.

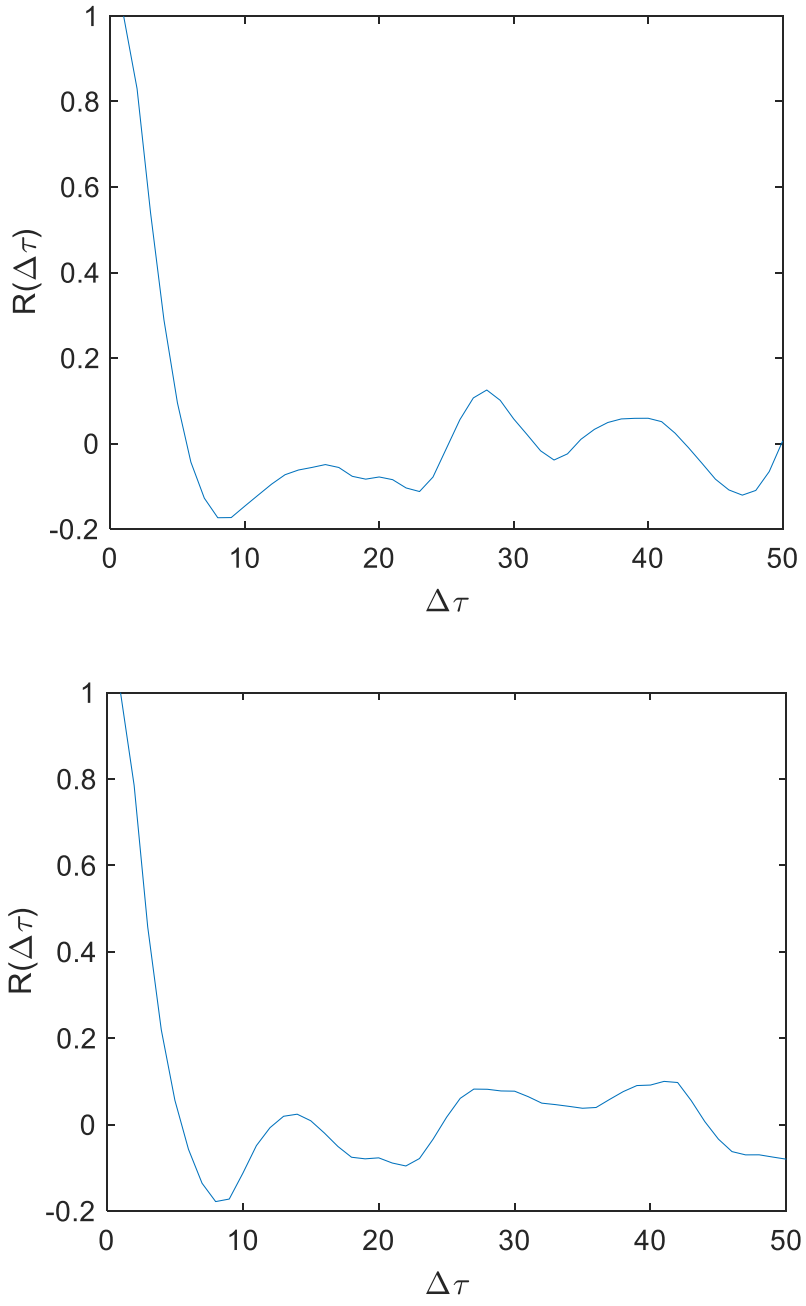

Fig. 11 Autocorrelation coefficient $R(\Delta\tau)$ for the axial liquid velocity at the height $h = 0.7$ m of the column at inlet superficial gas velocity $U_G = 6$ cm/s (top) and $U_G = 8.4$ cm/s (bottom).

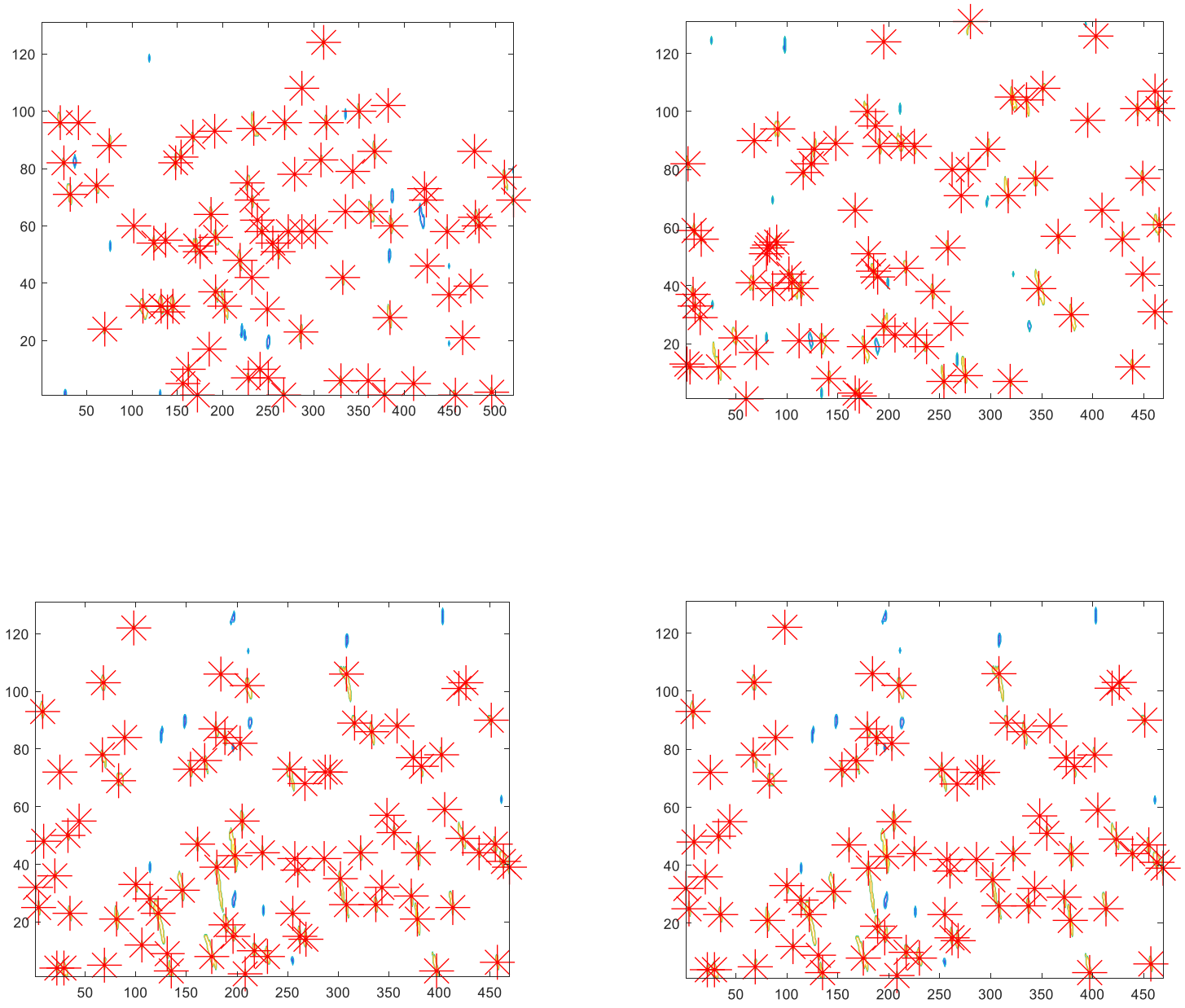

Fig. 12 Conditional sampled average flow structures map along the axial direction at each time at U_G cm/s (top) and $U_G = 8.4$ cm/s (bottom). The figures on the left-hand side correspond to template 1 and those on the right-hand side to template 2.

(a)

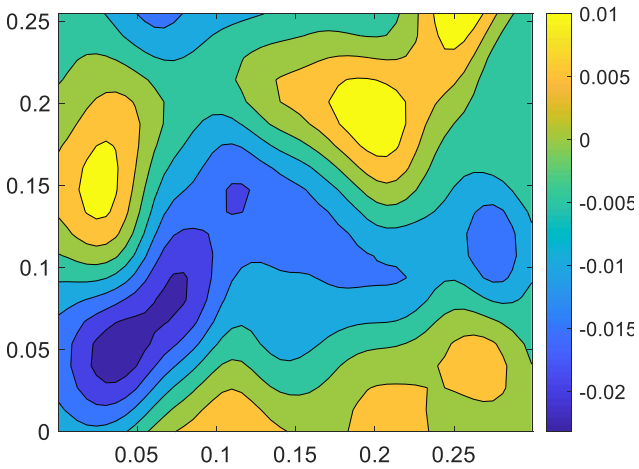
0.25
0.2
0.15
0.1
0.05
0
0.05
0.1
0.15
0.2
0.25
0.01
0.005
0
-0.005
-0.01
-0.015
-0.02

(b)

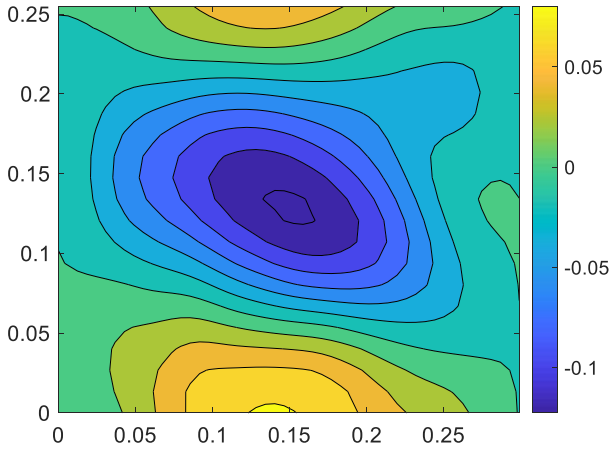
0.25
0.2
0.15
0.1
0.05
0
0
0.05
0.1
0.15
0.2
0.25
0.05
0
-0.05
-0.1

(c)

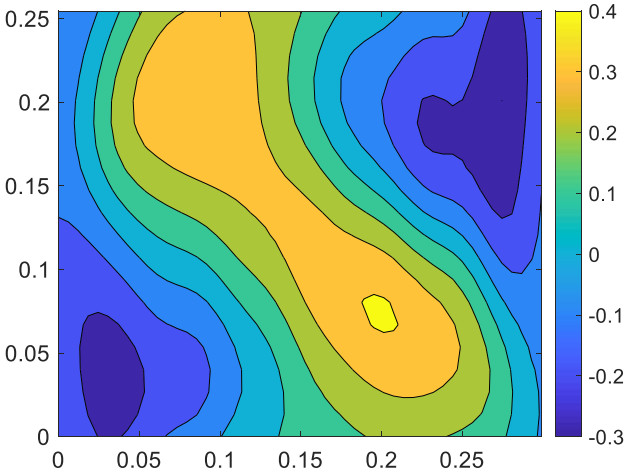
0.25
0.2
0.15
0.1
0.05
0
0
0.05
0.1
0.15
0.2
0.25
0.4
0.3
0.2
0.1
0
-0.1
-0.2
-0.3

(d)

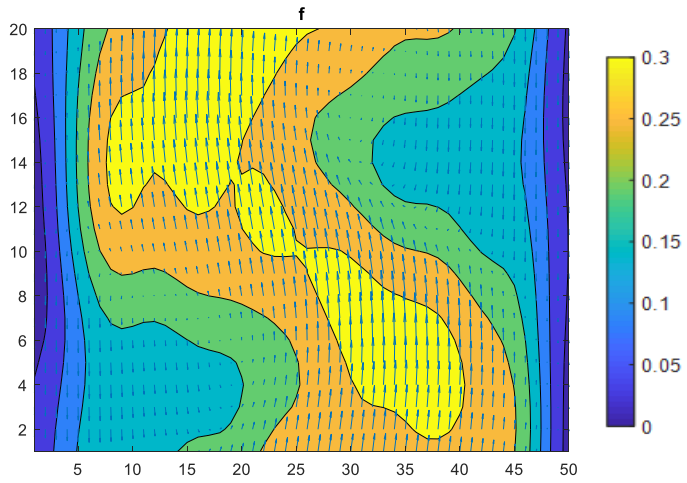
f
20
18
16
14
12
10
8
6
4
2
5
10
15
20
25
30
35
40
45
50
0.3
0.25
0.2
0.15
0.1
0.05
0

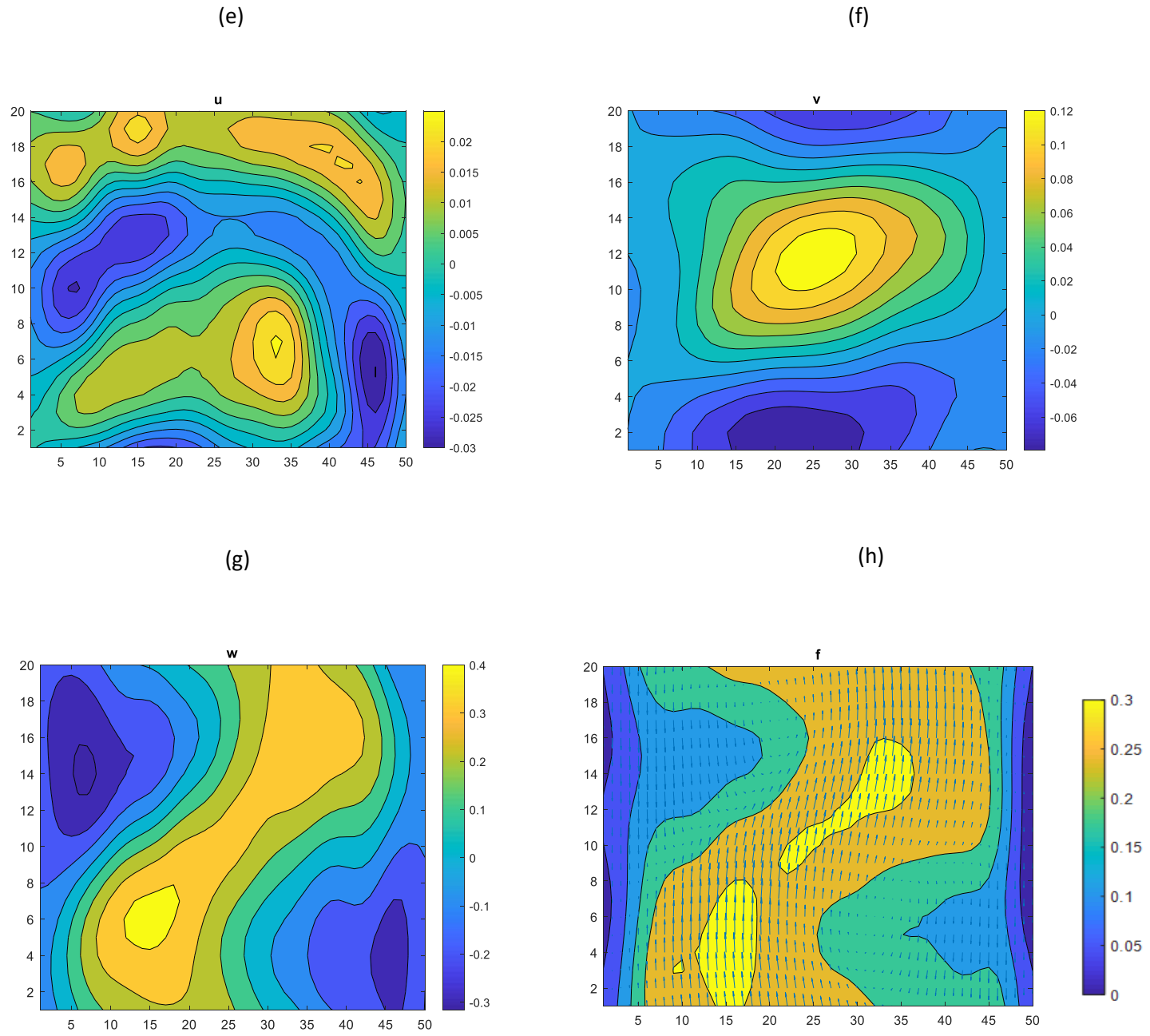

Fig. 13 Ensemble averaged of instantaneous liquid velocity and gas hold-up at $U_G = 6$ cm/s of (a, e) v −velocity, (b, f) u −velocity, (c, g) w −velocity, and (d, h) gas hold-up and vector field constructed with the axial and streamwise liquid velocity components. The figures (a)-(d) correspond to template 1 and (e)-(h) to template 2.

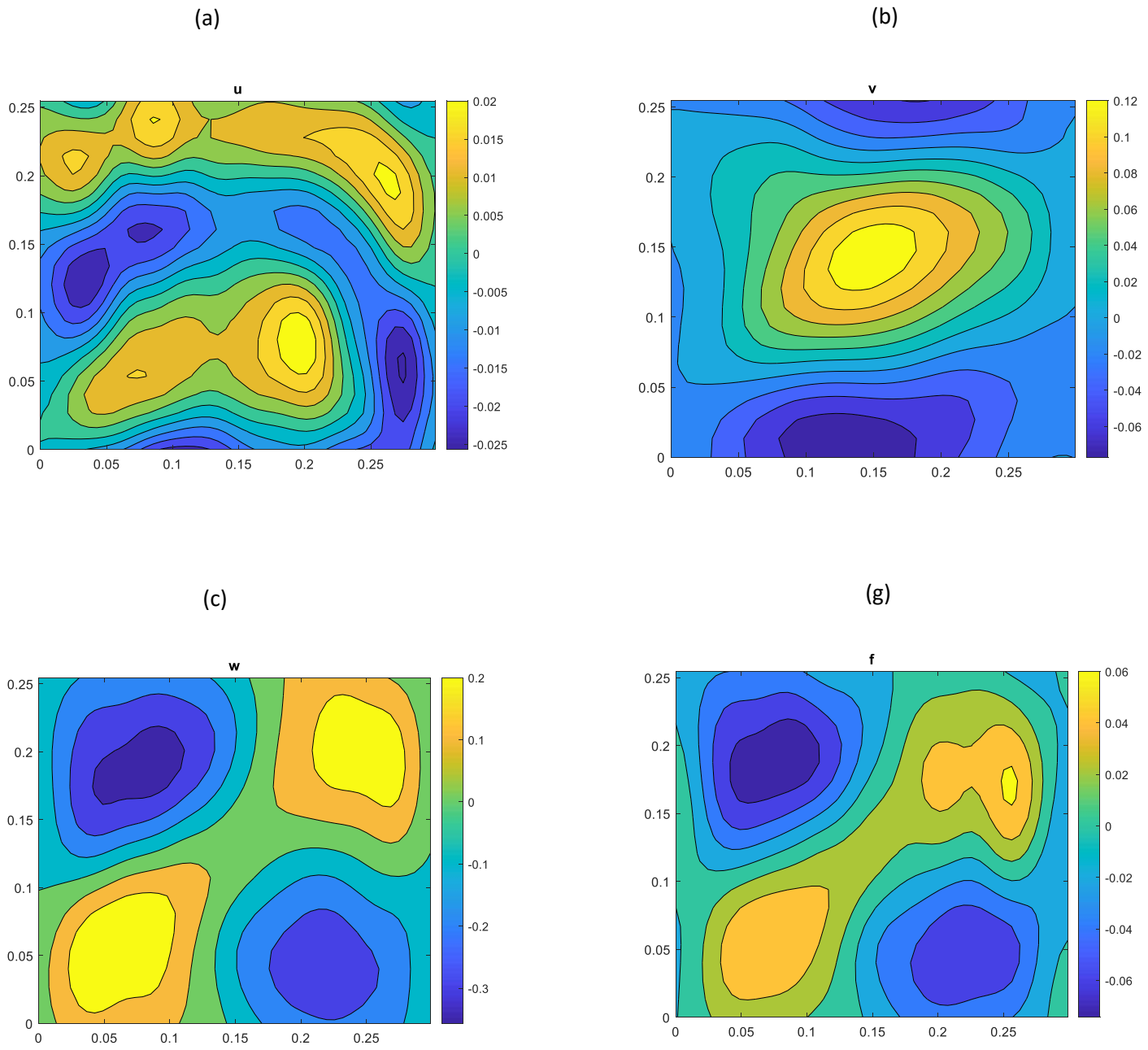

Fig. 14 Ensemble averaged of the fluctuation values at $U_G = 6$ cm/s of (a) v −velocity, (b) u −velocity, (c) w −velocity, and (d) gas hold-up.

(a)

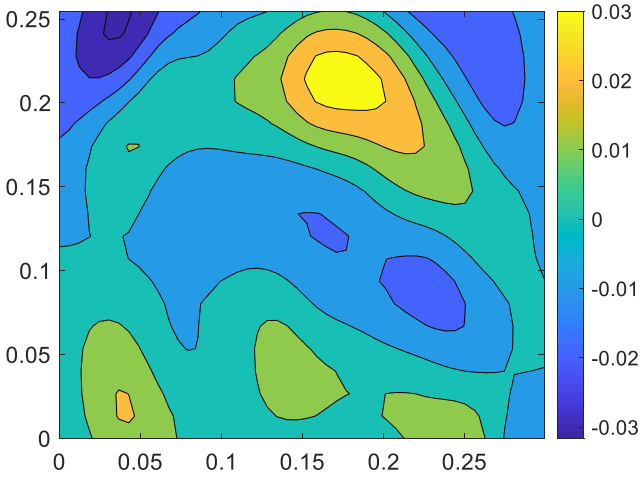
0.25
0.2
0.15
0.1
0.05
0
0 0.05 0.1 0.15 0.2 0.25
0.03
0.02
0.01
0
-0.01
-0.02
-0.03

(b)

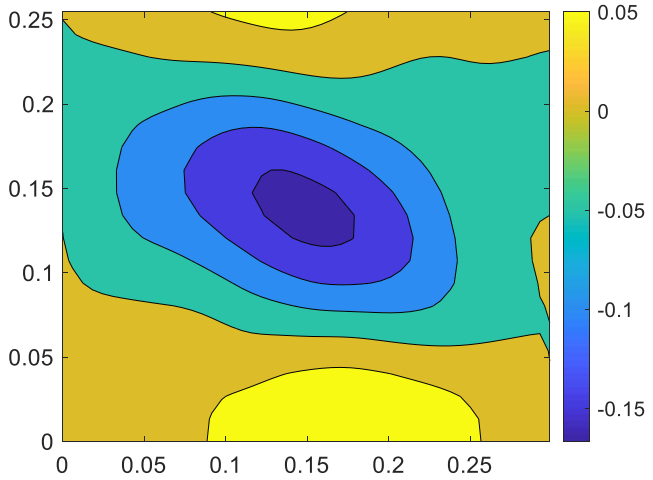
0.25
0.2
0.15
0.1
0.05
0
0 0.05 0.1 0.15 0.2 0.25
0.05
0
-0.05
-0.1
-0.15

(c)

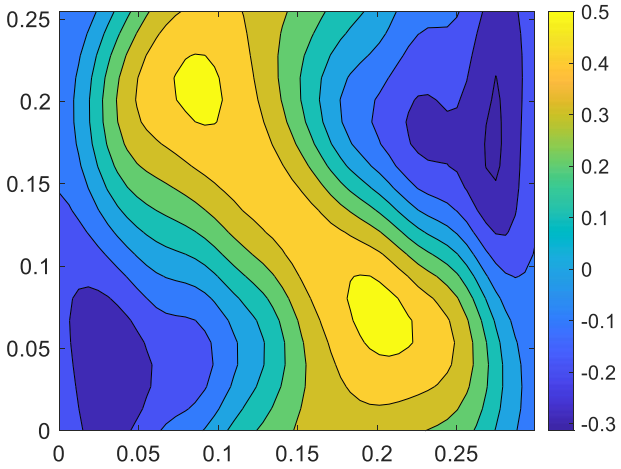
0.25
0.2
0.15
0.1
0.05
0
0 0.05 0.1 0.15 0.2 0.25
0.5
0.4
0.3
0.2
0.1
0
-0.1
-0.2
-0.3

(d)

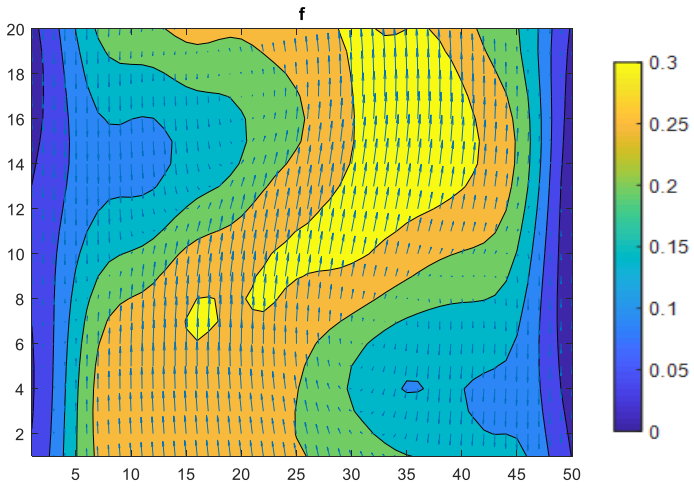
f
20
18
16
14
12
10
8
6
4
2
5 10 15 20 25 30 35 40 45 50
0.3
0.25
0.2
0.15
0.1
0.05
0

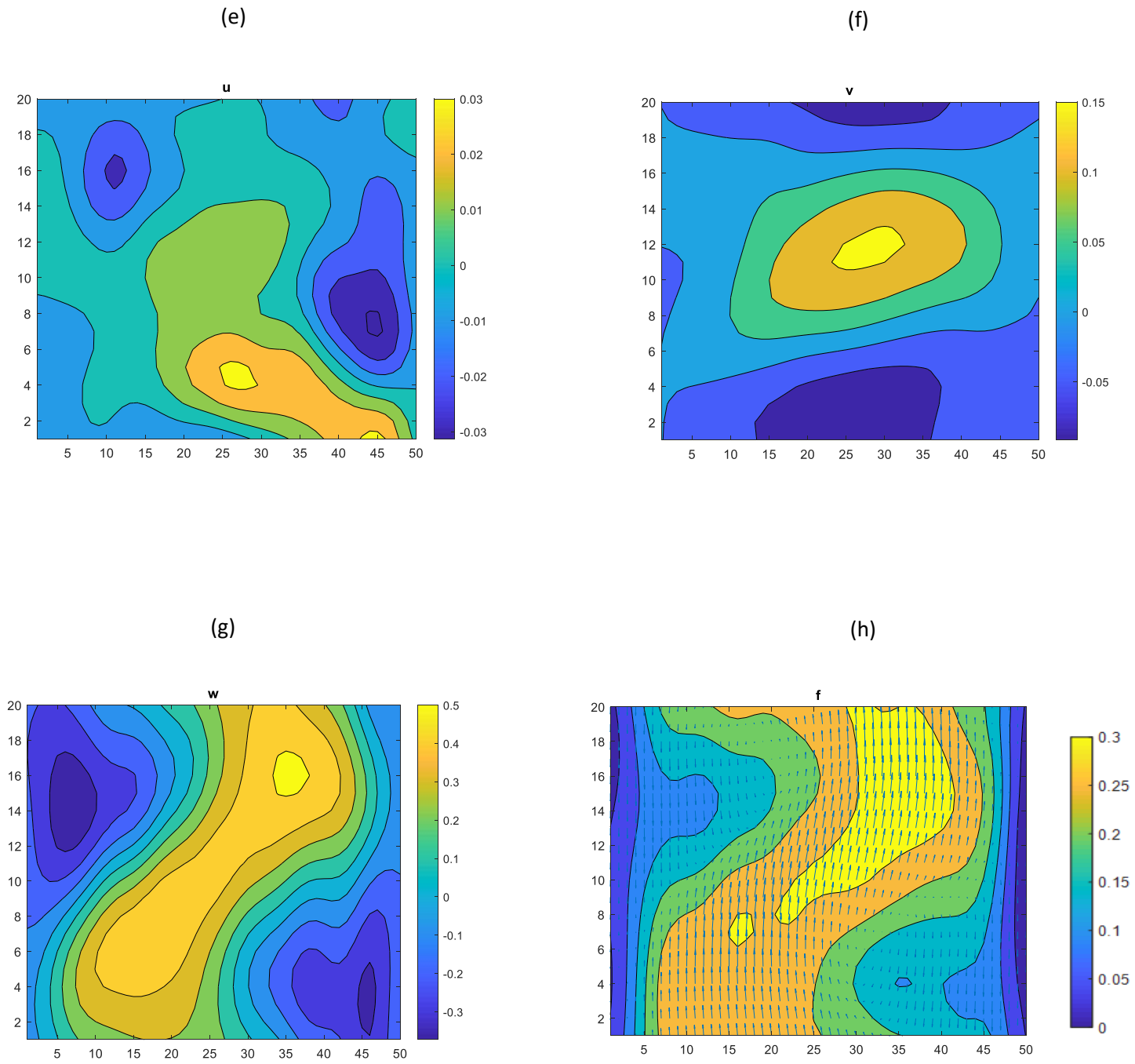

Fig. 15 Ensemble averaged of instantaneous liquid velocity and gas hold-up at $U_G = 8.4$ cm/s of (a, e) v −velocity, (b, f) u −velocity, (c, g) w −velocity, and (d, h) gas hold-up and vector field constructed with the axial and streamwise liquid velocity components. The figures (a)-(d) correspond to template 1 and (e)-(h) to template 2.

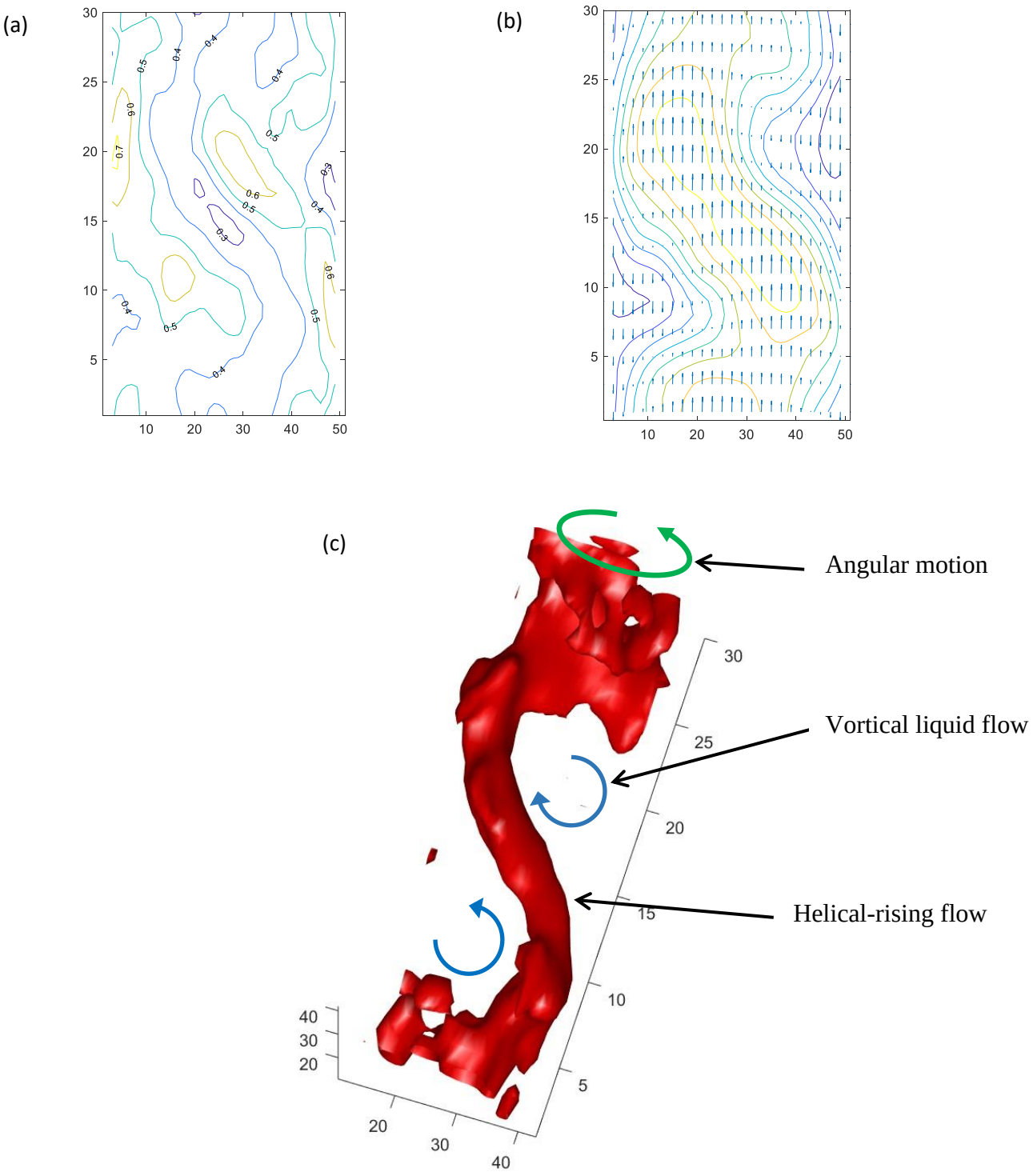

Fig. 16 (a) Sectional streamlines pattern, (b) ensemble average of ω_y with vector field constructed with the axial and streamwise liquid velocity components, (c) and three-dimensional view of vorticity iso-surface $|\omega| = 0.4\ |\omega_{\max}|$ at $U_G = 6$ cm/s.

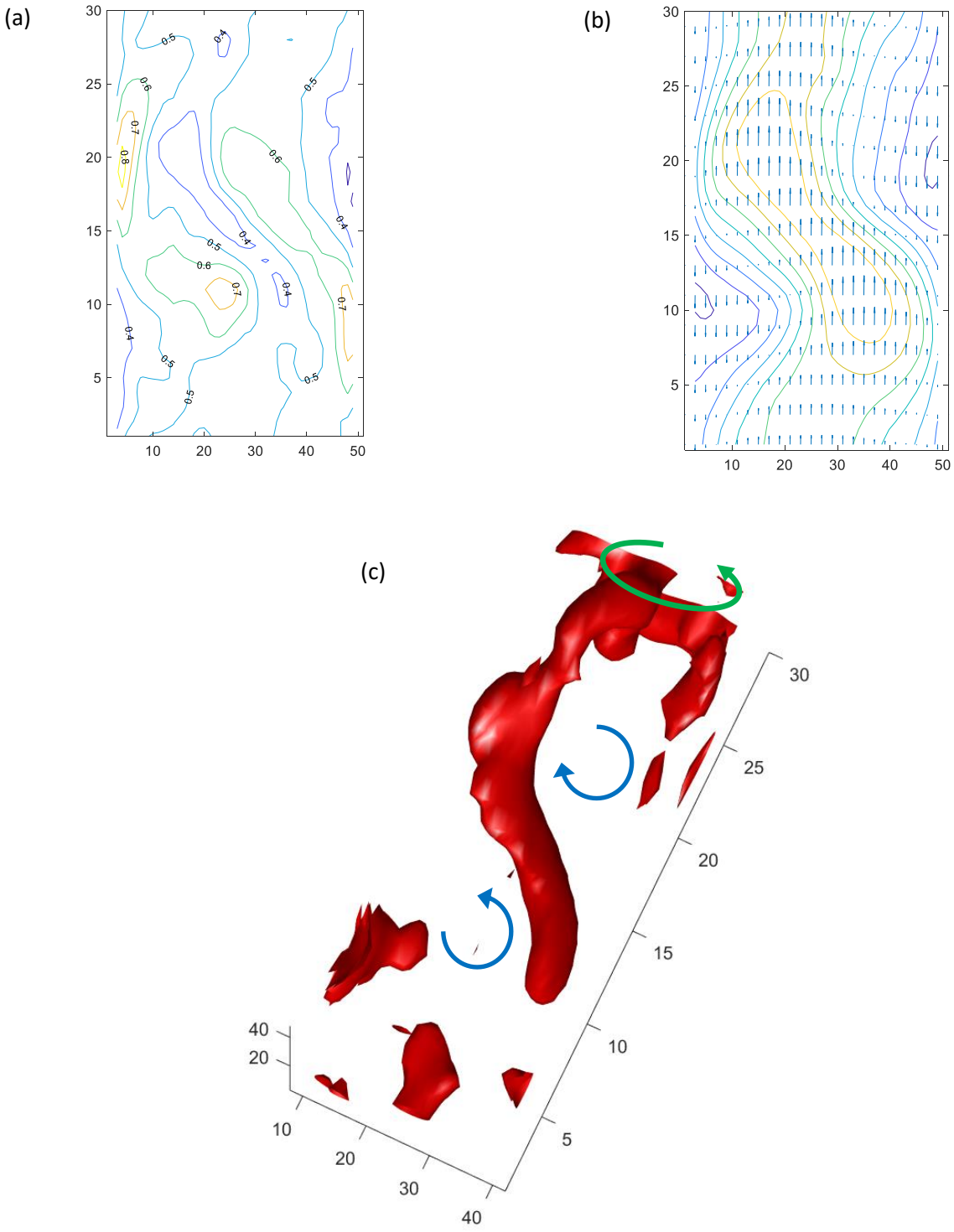

Fig. 17 (a) Sectional streamlines pattern, (b) ensemble average of ω_y with vector field constructed with the axial and streamwise liquid velocity components, and (c) three-dimensional view of vorticity iso-surface $|\omega| = 0.45\ |\omega_{\max}|$ at $U_G = 8.4$ cm/s.